Engineering Applications of Non-smooth Dynamics

Marian Wiercigroch and Ekaterina Pavlovskaia

Abstract. This chapter introduces and discusses practically important concept of non-smooth dynamical systems, which are very common in engineering applications. Mathematically, such systems can be considered as piecewise smooth and therefore their global solutions are obtained by stitching local solutions, which are easy to develop by standard methods. If a dynamical system is piecewise linear then an implicit global analytical solution can be given, however the times when non-smoothness occurs have to be determined first. This leads to a set of nonlinear algebraic equations. To illustrate the non-smooth dynamical systems and the methodology of solving them, three mechanical engineering problems were studied. Firstly, a vibro-impact system in a form of moling device was modelled and analysed to understand how the progression rates can be maximised. For this system, periodic trajectories can be reconstructed as they go through three linear subspaces (no contact, contact with progression and contact without progression), and using combination of analytical and numerical methods the optimal range of the system parameters can be identified. In the second application the influence of opening and closing of a fatigue crack on the system dynamics was investigated. Specifically, a novel apparatus to induce aperiodic loading to a specimen with a fatigue crack was studied. It was shown experimentally that fatigue life can be reduced few times if the sample is loaded aperiodically. The analysis of the developed mathematical model shown that as a crack grows linearly before reaching its critical value, the response of the system remains periodic. When its size exceeds the critical value, the system behaviour becomes chaotic and then the crack growth increases exponentially. This phenomenon can be used in structural health monitoring. The last problem comes from rotordynamics, where nonlinear interactions between the rotor and the snubber

Marian Wiercigroch · Ekaterina Pavlovskaia
Centre for Applied Dynamics Research, School of Engineering,
Aberdeen University, King's College, AB24 3UE, Aberdeen, Scotland, UK
e-mail: {m.wiercigroch,e.pavlovskaia}@abdn.ac.uk

J. Warminski et al. (Eds.): Nonlinear Dynamic Phenomena in Mechanics, SMIA 181, pp. 211–273.
springerlink.com

ring were studied. The influence of the preloading of the snubber ring on the system behaviour was investigated and the range of the system parameters where chaotic vibrations occur was identified. The results obtained from the developed mathematical model confronted with the experiments shown a good degree of correlation.

Keywords: Non-smooth dynamics, vibrations, mechanical systems, vibro-impact moling, fatigue, rotor systems.

1 Non-smooth Dynamical Systems in Engineering Dynamics [56, 60, 44, 58, 59]

Most of engineering systems are inherently nonlinear and their nonlinearities manifest themselves in many different forms, where one of the most common is the non-smoothness. One may think of the noise of a squeaking chalk on a blackboard, or more pleasantly of a violin concert. Mechanical engineering examples include squeal in brakes, impact print hammers, percussion drilling machines or chattering of machine tools. These effects are due to the non-smooth characteristics such as clearances, impacts, intermittent contacts, dry friction, or combinations of them [60].

Non-smooth dynamical systems have been extensively studied for nearly four decades showing a huge complexity of dynamical responses even for a simple impact oscillator or Chua's circuit. The theory of non-smooth dynamical systems has been rapidly developing and now we are in much better position to understand those complexities occurring in the non-smooth vector fields and caused by generally discontinuous bifurcations. There are numerous practical applications, where the theoretical findings on nonlinear dynamics of non-smooth systems have been applied in order to verify the theory and optimize the engineering performance. However, from a mathematical point of view, problems with non-smooth characteristics are not easy to handle as the resulting models are dynamical systems whose right-hand sides are discontinuous [14], and therefore they require a special mathematical treatment and robust numerical algorithms to produce reliable solutions. Therefore, we apply a combination of numerical, analytical and semi-analytical methods to analyse such systems and this particular aspect will be a focus in this chapter.

Many characteristics of mechanical systems can be non-smooth, and such systems mathematically can be described as so-called piecewise smooth dynamical systems. Well-known examples include an impact oscillator (e.g. [49]), piecewise linear oscillators (e.g. [46, 51, 41, 63]), mechanical "bouncing ball" system [64], Jeffcott rotor with bearing clearances [33, 45, 22], systems with Coulomb friction (e.g. [13, 55]), gear-box systems [29, 38, 12] and metal cutting processes [23, 57]. A general methodology proposed in [56, 44, 58] of describing and solving non-smooth dynamical system which originates from the Fillipov's approach [14] can be found for example in [60] and [37]. It includes modelling of discontinuous systems by discontinuous functions and by smooth functions. In the latter case extra care is required as smoothing discontinuities can produce an artifact responses [32]. Here

the first approach will be adopted, where a dynamical system is defined in global hyperspace Ω as continuous but not necessarily smooth autonomous system [56]

$$\dot{\mathbf{x}} = \mathbf{f}(\mathbf{x}, \mathbf{p}), \tag{1}$$

where $\mathbf{x} = [x_1, x_2, \ldots, x_n]^T$ is the state space vector (x_n is used to represent time), $\mathbf{p} = [p_1, p_2, \ldots, p_m]^T$ is a vector of the system parameters, and $\mathbf{f}(\mathbf{x}, \mathbf{p}) = [f_1, f_2, \ldots, f_n]^T$ is the vector function which is dependent upon the system structure or the process being modelled. Then we assume that the dynamical system (1) is smooth but only within subspace $\mathbf{X}_i$ of the global hyperspace Ω (see Fig. 1). Therefore, for each subspace $\mathbf{X}_i$ ($\mathbf{x} \in \mathbf{X}_i$), the right hand side of equation (1) may be described by a different function, $\mathbf{f}_i(\mathbf{x}, \mathbf{p})$ where $i \in [1, N]$. Such system description will be used throughout this chapter where for each individual problem we will specify global and local subspaces which will define its regimes of operations.

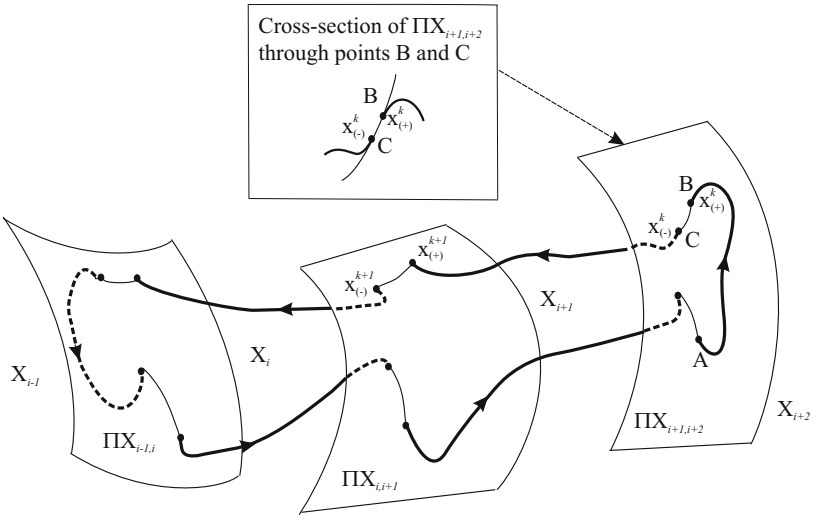

Fig. 1 Conceptual model of a piecewise smooth dynamical system, where thick lines (solid and dash) denote trajectories within subspaces and thin lines – trajectories sliding on the hypersurfaces [44]

The main aim of this chapter is to outline a general methodology of modelling and analysing of non-smooth dynamical systems. The methodology will be illustrated through three case studies. Firstly, the dynamics of a drifting vibro-impact system will be investigated through a novel semi-analytical method developed in [46, 42, 48, 61, 43, 47, 44], which allows to determine the favourable operating conditions. The model accounts for visco-elastic impacts and is capable to mimic dynamics of progressive motion (a drift). Secondly, we will study the evolution of a fatigue crack in a specimen subjected to aperiodic loading [18, 15, 16, 19, 17]. A

unique experimental rig developed to investigate the dynamic crack growth under aperiodic excitation will be briefly discussed and then the modelling of the crack growth embedded into the mechanical model of the entire system will be shown. A comparison between the theoretical and experimental results will verify the model. Finally, we will examine the complex dynamics of a rotor system with bearing clearances [33, 32, 30, 31, 45, 34], where a contact incident is modelled as a piecewise smooth effect. Influence of the preloading of the snubber ring on the dynamic responses and the comparison with the experiments will be discussed.

2 Drifting Oscillator as an Effective Model of Vibro-impact Moling [48]

Vibro-impact systems are strongly nonlinear and have been widely used in civil and mechanical engineering applications. These include ground moling machines, percussive drilling, ultrasonic machining and mechanical processing (cold and hot forging). Let us focus here on a vibro-impact system driving a pile into the ground, where during its operation the driving module moves downwards, and its motion can be viewed as a superposition of a progressive motion and bounded oscillations. The simplest physical model exhibiting a such behaviour is comprised of a mass loaded by a force having static and harmonic components, and a dry friction slider, as shown in Fig. 2(a). This model was introduced and preliminary analysed in [35, 36]. Despite its simple structure, a very complex dynamics was revealed. The main result from that work was the finding that the best progression occurs during period one responses. A more realistic model including viscoelastic properties of the ground and its optimal periodic regimes were studied extensively in [46, 42, 48, 61, 43, 47, 44].

2.1 Mathematical Modelling and Experimental Study

A simple model of a vibro-impact moling system may be represented as an oscillating mass with a frictional visco-elastic slider, as shown in Fig. 2(b). This model defines the motion of the moling device (mass) and the soil (slider) which allows to make a distinction between the motion of the mole head and the front face of the hole.

The model of the soil represented by a frictional slider is depicted in Fig. 3(a). The dependence of the soil resistance on the penetration of the tool for this model is marked by a solid line in Fig. 3(b). This dependence is similar to one obtained by Spektor [54], who approximated it by a piece-wise linear relationship. The other approach used in the previous studies [50] considered the overall soil resistance as a superposition of the frontal elasto-plastic force (dash line in Fig. 3(b)) and the viscous damping force created by the fluidized soil.

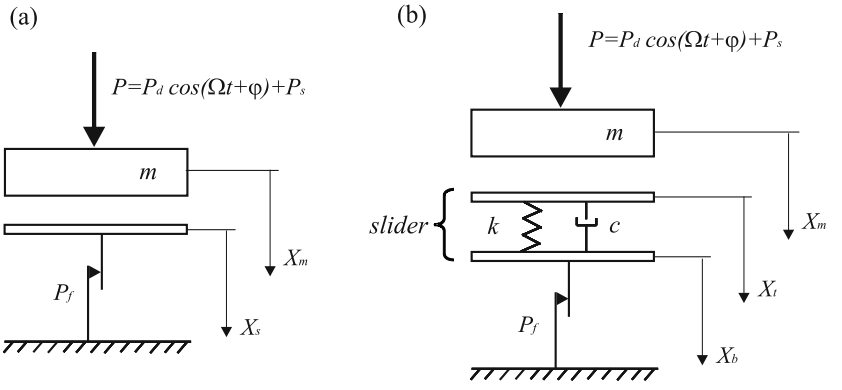

Fig. 2 Physical models of progressive impact systems; **a** simplest models [35, 36], **b** more realistic model [46]

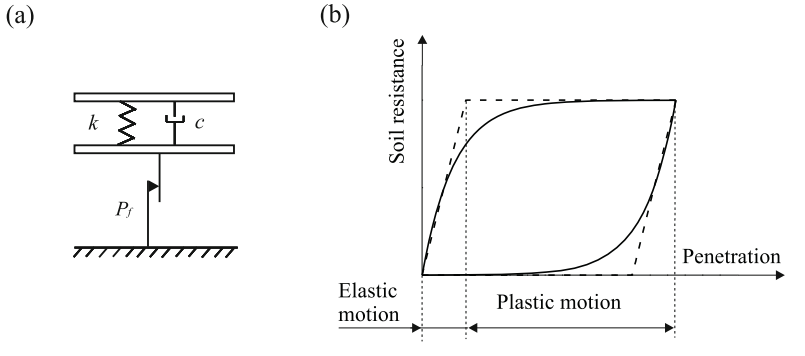

Fig. 3 Model of soil [48]; **a** physical model as a frictional slider with elasticity and viscous damping, **b** soil resistance versus penetration characteristics

In order to gain some insight into the dynamics of vibro-impact moling systems, a brief experimental study was carried out on the rig depicted in Fig. 4, which was originally designed by Lok *et al.* [39]. It comprises a steel tube hosting an oscillatory mass. The vibro-impact mechanism is comprised of a vibratory mass and a hammer mass both supported by coil springs. The hammer mass impacts upon the nose cone. The springs are precompressed in the tube and the excitation is provided by a cam driven system with a variable rotational speed.

As can be seen from Fig. 4 the moling system is set to operate in a sand box. The relative displacement of the mole with respect to the sand box was measured by an

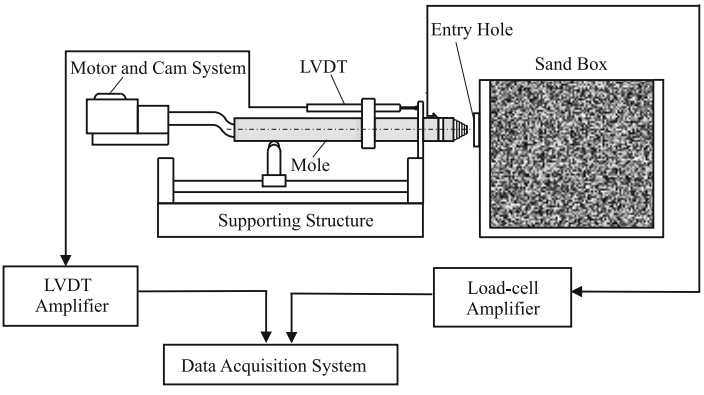

Fig. 4 Schematic of the experimental set-up to study the dynamics of vibro-impact ground moling system [48]

LVDT. The recorded signal was passed through an amplifier and monitored by an oscilloscope before being captured on a data storage system. A circular strain gauge load-cell was fitted between the impacting mass and the nose cone to measure the impact forces.

In spite of its very simple structure the model confirms the main phenomena occurring during the soil-penetrator interactions. In Fig. 5 the experimental (a, c) and the numerical (b, d) results are compared. As can be seen, there is a good qualitative agreement between the time histories. This similarity allows us to draw a conclusion that this simple model can be used to study the soil-mole dynamic interactions.

In the considered model shown in Fig. 2(b) a mass m is excited by an external force comprised of a harmonic component of amplitude P_d, frequency Ω and phase shift φ; and a static component, P_s. The slider has weightless top and bottom plates connected to each other by a linear spring with stiffness k, and a viscous damper with damping coefficient c. The progressive motion of the mass occurs when the force acting on the slider exceeds the threshold of the dry friction force, P_f. X_m, X_t and X_b represent the absolute displacements of the mass, slider top and slider bottom respectively.

For the case when the mass and the slider move separately the dynamics of the system is described by one second and two first order differential equations

$$\begin{cases} m\ddot{X}_m = P_s + P_d \cos(\Omega t + \varphi), \\ c\left(\dot{X}_t - \dot{X}_b\right) + k\left(X_t - X_b\right) = 0, \\ \dot{X}_b = 0. \end{cases} \tag{2}$$

The case when the mass and the slider are in contact, is described by one second order and one first order differential equations, which can be either oscillatory

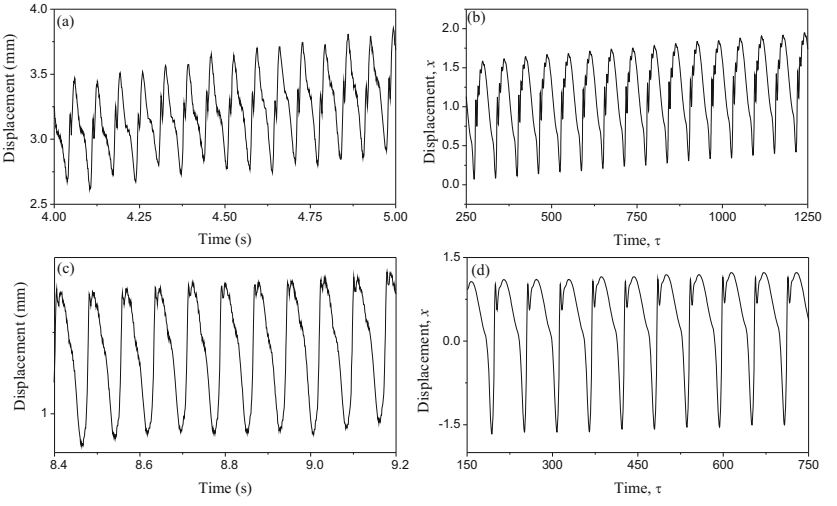

Fig. 5 **a**, **c** Experimental data [48] obtained from the rig with a double cam of 4 mm lift rotating at 7.75 Hz and effectively inducing a forcing frequency of **a** 15.5 Hz and **c** 13.2 Hz; **b**, **d** Results of numerical simulation for **b** $a = 0.5,\ \omega = 0.11,\ \xi = 0.35,\ b = 0.456$, and for **d** $a = 0.5,\ \omega = 0.1,\ \xi = 0.11,\ b = 0.48$

$$\begin{cases} m\ddot{X}_m + c\left(\dot{X}_t - \dot{X}_b\right) + k\left(X_t - X_b\right) = P_s + P_d\cos(\Omega t + \varphi), \\ \dot{X}_b = 0, \end{cases} \tag{3}$$

or progressive

$$\begin{cases} m\ddot{X}_m = -P_f + P_s + P_d\cos(\Omega t + \varphi), \\ c\left(\dot{X}_t - \dot{X}_b\right) + k\left(X_t - X_b\right) = P_f. \end{cases} \tag{4}$$

Note that for Eqs. (3) and (4) the displacement of the slider top, X_t is in phase with the displacement of the mass, X_m, but differs by a gap, G (G is the distance between the mass and the slider top at the initial point $t = 0$)

$$X_t = X_m - G.$$

The equations of motion (2) – (4) are transformed to a system of first order differential equations by using the following non-dimensional variables

$$\tau = \Omega_0 t,\ \ x = \frac{k}{P_{max}}X_m,\ \ y = \frac{dx}{d\tau} = \frac{k}{\Omega_0 P_{max}}\dot{X}_m,$$

$$z = \frac{k}{P_{max}}X_t,\ \ v = \frac{k}{P_{max}}X_b,$$

and parameters

$$\omega = \frac{\Omega}{\Omega_0}, \quad \Omega_0 = \sqrt{\frac{k}{m}}, \quad a = \frac{P_d}{P_{max}}, \quad b = \frac{P_s}{P_{max}},$$

$$d = \frac{P_f}{P_{max}}, \quad \xi = \frac{c}{2m\Omega_0}, \quad g = \frac{k}{P_{max}}G.$$

The considered system can operate at any time in one of the following modes:

- No contact,
- Contact without progression,
- Contact with progression.

For the simplicity of further analysis, the dimensionless friction threshold force, d is set to 1. We also assume the parameters $g = 0.02$ and $\varphi = \pi/2$ to be constant in this study. Consequently, Eqs. (2) – (4) can be formulated for these specified modes in the first order ODEs.

If the displacement of the mass is smaller than the displacement of the slider top plus the gap,

$$x < z + g, \tag{5}$$

then the mass and the slider top move separately. The motion of the mass can be determined from the following set of equations

$$\begin{cases} x' = y, \\ y' = a\cos(\omega\tau + \varphi) + b, \end{cases} \tag{6}$$

where $'$ denotes $d/d\tau$. The equations of motion for the top and the bottom of the slider are

$$z' = -\frac{1}{2\xi}(z - v), \tag{7}$$

$$v' = 0. \tag{8}$$

Contact without progression occurs when the relative displacement of the mass exceeds the displacement of the slider top plus the gap, i.e.

$$x \geq z + g, \tag{9}$$

and the force acting on the mass from the slider is greater than zero but smaller than the threshold of the dry friction force, which can be expressed as

$$0 < 2\xi z' + (z - v) < 1. \tag{10}$$

In this case the mass and the slider top move together but without progression, and the second equation of (6) has additional elastic and viscous terms:

$$\begin{cases} x' = y, \\ y' = -2\xi z' - (z - v) + a\cos(\omega\tau + \varphi) + b. \end{cases} \tag{11}$$

The velocity of the slider top is equal to the velocity of the mass, and the displacement of the slider top is in phase with the mass displacement but differs by g in position

$$z' = x', \tag{12}$$

$$x = z + g. \tag{13}$$

When there is no progression, the bottom of the slider remains stationary, hence its velocity is equal to zero

$$v' = 0. \tag{14}$$

When the displacement of the mass is equal or greater than the displacement of the slider top plus the gap (see Eq.(9)), and the force acting on the mass is greater than the threshold of dry friction force

$$2\xi z' + (z - v) \geq 1, \tag{15}$$

then the mass and the top and the bottom of the slider are moving together, and progression takes place. The equations of motion for mass are

$$\begin{cases} x' = y, \\ y' = a\cos(\omega\tau + \varphi) + b - 1. \end{cases} \tag{16}$$

The displacement and the velocity of the slider top are described as before (see Eqs. (12) and (13)). The velocity of the slider bottom motion can be calculated from the expression below

$$v' = z' + \frac{1}{2\xi}(z - v - 1). \tag{17}$$

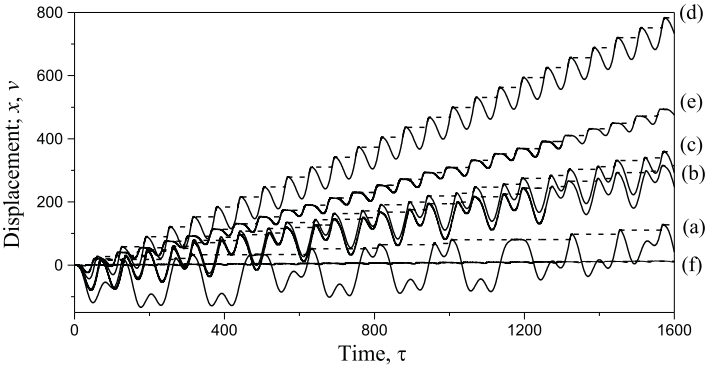

Fig. 6 Time histories [46] of the mass, x (solid curves) and slider bottom, v (dash curves) calculated for $a = 0.3,\ \omega = 0.1,\ \xi = 0.05$ and (a) $b = 0.05$; (b) $b = 0.095$; (c) $b = 0.1$; (d) $b = 0.15$; (e) $b = 0.19$ and (f) $b = 0.27$

Equations (5)–(17) were used to conduct an extensive nonlinear dynamic studies by means of numerical simulation using *Dynamics* software [65], and also to develop an algorithm to determine periodic responses [46, 42].

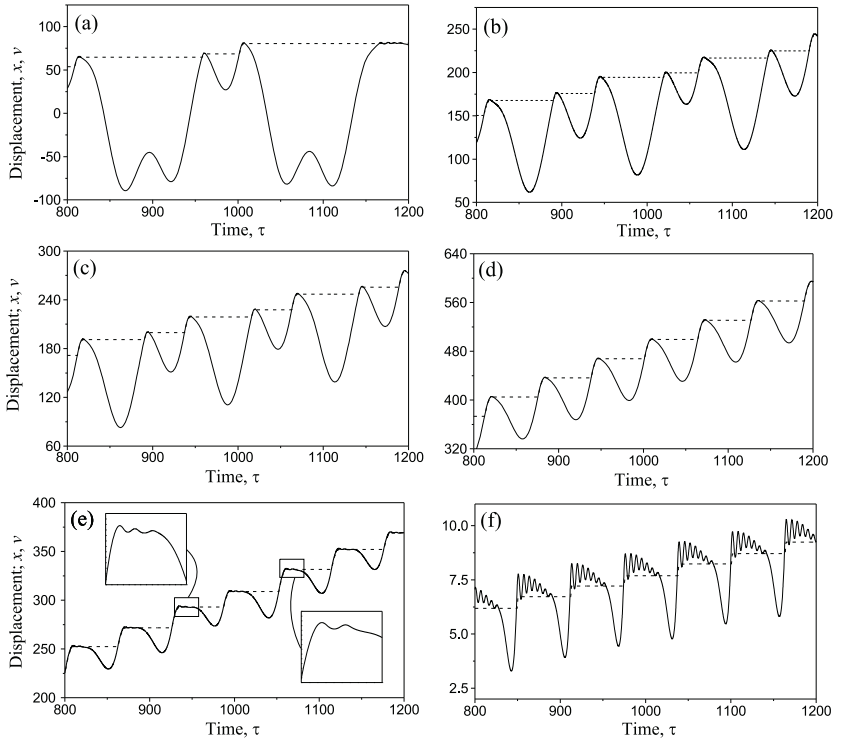

Fig. 7 Time histories of steady-state responses [46] of the mass, x (solid curves) and slider bottom, v (dash curves) for $a = 0.3,\ \omega = 0.1,\ \xi = 0.05$ and **a** $b = 0.05$; **b** $b = 0.095$; **c** $b = 0.1$; **d** $b = 0.15$; **e** $b = 0.19$ and **f** $b = 0.27$

Our study has revealed that the best progression (the largest drift) is achieved for the period one motion, which can be clearly seen by examining displacement of the slider bottom (dash lines) in Fig. 6. These steady-state responses are also depicted in Fig. 7(a)-(e) for $\tau \in (800,\ 1200)$. Figure 7 shows an important sequence of subcritical bifurcations, where the system bifurcates from a period four (Fig. 7(b)) to a period two (Fig. 7(c)), then from a period two to a period one (Fig. 7(d)). A transition from a period one to a chaotic motion with a high frequency component (Fig. 7(e)) determines the interval of static force, b, for which the best progression exists. The system can also exhibit chaos for a wide range of the system parameters (e.g. see Fig. 8(a)).

2.2 Determination of the Best Progression

Figure 8 demonstrates a number of bifurcation diagrams showing the velocity and progression of the system as function of the static force for different values of the dynamic amplitude. As can be seen in Fig. 8(a)-(c) the system responds aperiodically for small values of static force, b with some narrow windows of periodic motion. This is followed by a large window of periodic motion marked by dash lines, which is increasing for the larger values of dynamic force, a. Then a series of aperiodic and periodic windows appear. It should be noted that if the dynamic force, a, is large the system responds periodically for the most values of the static force, b (Fig. 8(c)).

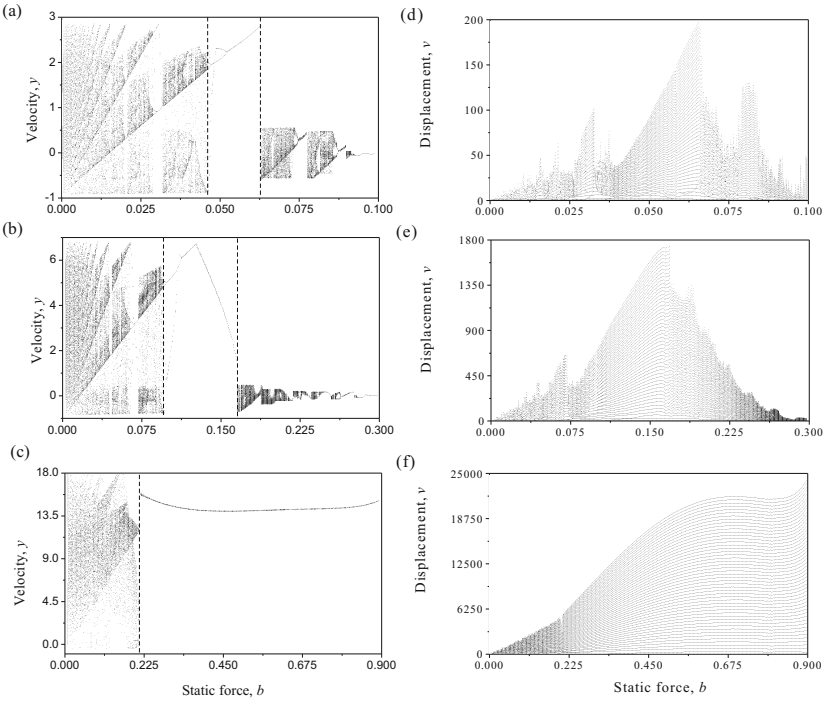

Fig. 8 Bifurcation diagrams [48] $y = y(b)$ and progression during the first 50 periods respectively for $\xi = 0.05$, $\omega = 0.1$ and **a**, **d** $a = 0.1$; **b**, **e** $a = 0.3$; and **c**, **f** $a = 0.9$

The analysis of the bifurcation diagrams has also unveiled some insight regarding the progression rates achieved by the system. It was obtained that the best progression is reached when system responds periodically with the period of external excitation. As can be clearly seen from Fig. 8(d)-(f), the maximum penetration rate coincides with the point where periodic regime becomes aperiodic. For a special case of large dynamic force, $a = 0.9$, shown in Fig. 8(f), we have periodic regimes

for all values of static force, b starting from $b \approx 0.225$, and the progression rate increases starting from this value of static force, b. In general, as the system is essentially nonlinear, better progression rates are not necessarily achieved for larger static forces.

The finding regarding the position of the maximum penetration rate (the end of periodic regime) was used to develop a semi-analytical algorithm for determining this point and details can be found in [42]. This method constructs a periodic response assuming that each period is comprised of a sequence of distinct phases for which analytical solutions are explicitly known. For example, a period may consist of the following sequential phases: Contact with progression, Contact without progression, No contact and Contact without progression. Using this information a system of four piecewise linear first order differential equations is transformed to a system of nonlinear algebraic equations. Then an accurate prediction of the range of control parameters for which the best progression rates are obtained, can be made without laborious numerical simulation.

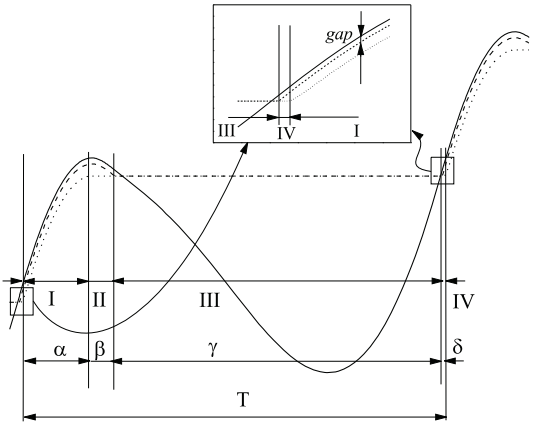

Fig. 9 Four stages of a periodic response [46]; solid line – displacement of the mass, dash line – displacement of the slider top, dotted line – displacement of the slider bottom. The blow-up window shows the displacements of the mass, slider top and bottom at the beginning and at the end of the period

As our system is piecewise linear, the periodic solutions can be constructed by stitching linear solutions obtained in the subspaces at points of discontinuities. Initially, it is assumed that the displacement and velocity of the mass have certain (as yet unknown) values. Starting from these values, the system operates in one of the phases described earlier. For the period one motion it goes through a sequence of four phases as presented in Fig. 9. As mentioned earlier a typical pattern is comprised of Contact with progression (Phase I), Contact without progression (Phase II), No contact (Phase III) and again Contact without progression (Phase IV). The

solutions for each phase are constructed by allowing the final displacements and velocities of the preceding phase to be the initial conditions for the next phase. The initial conditions of the first phase are determined from the periodicity condition.

In order to simplify our consideration, the beginning of progression was chosen as an initial point. Based on Eqs. (12), (13) and (15), the following relation between the initial displacement and velocity can be written

$$2\xi y_0 + (x_0 - g - v_0) = 1. \tag{18}$$

As the initial displacement of the slider bottom, v_0 does not influence the motion of the mass, it is set to zero. Then we have

$$x_0 = 1 + g - 2\xi y_0. \tag{19}$$

The other unknown is a phase shift, ψ_0, between the external force and the system response at the beginning , $\tau = \tau_0$

$$\psi_0 = \varphi + \omega\tau_0. \tag{20}$$

Two periodic conditions for the mass displacement and velocity can be established

$$\begin{cases} x(\tau + T) = x(\tau) + \Delta, \\ y(\tau + T) = y(\tau), \end{cases} \tag{21}$$

where T is the period equal to the period of external forcing

$$T = \frac{2\pi}{\omega}, \tag{22}$$

and Δ is progression of the slider per period.

Thus three unknown functions ψ_0, x_0 and y_0 can be determined from the equations (21) and (22). However an arbitrary solution of these equations cannot guarantee that x_0 and y_0 satisfy Eq.(19). For this reason we first substitute x_0 by the function of y_0 (expression Eq.(19)), and then construct a special function F to monitor a difference between the exact periodic solution and the one calculated for these arbitrary initial conditions

$$F = \sqrt{(x(\tau + T) - x(\tau) - \Delta)^2 + (y(\tau + T) - y(\tau))^2}. \tag{23}$$

If the minimum of this function is equal to zero, then the periodic regime exists, and the durations of all four stages can be determined. More details can be found in [42].

The results obtained using this method are presented in Fig. 10 showing the influence of the frequency, the dynamic force and the static force on the progression per period. It can be deduced from Fig. 10(a) that a better progression can be achieved for a smaller excitation frequency. Here a number of values of the dynamic amplitude was considered, and the monotonically decreasing curves indicate higher

penetration rates for larger amplitudes. From Fig. 10(b), it is seen that the larger the dynamic and static force are, the larger the progressions per period are obtained. Figure 10(c) shows that the progression reaches a maximum value at some certain values of static force and close to this maximum the periodic solution breaks down. The parts of the curves represented by dash lines are calculated using the same algorithm, however for these values of static force the motion detected is not periodic.

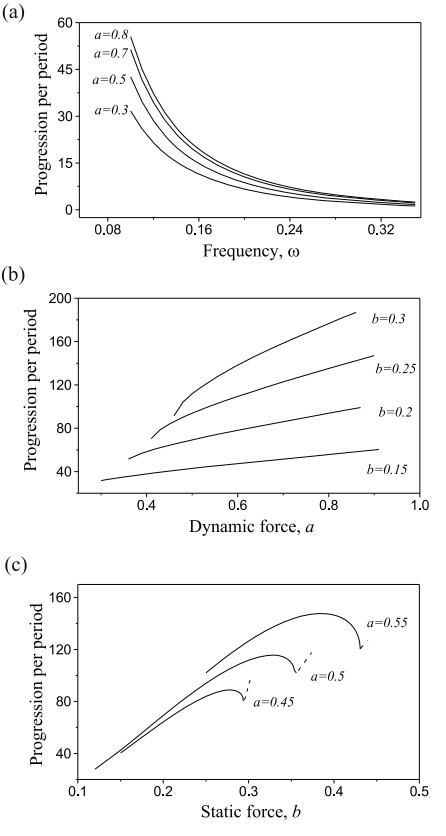

Fig. 10 Progression per period as a function of **a** frequency ω for $\xi = 0.01,\ b = 0.15$; **b** dynamic force a for $\omega = 0.1,\ \xi = 0.01$; **c** static force b for for $\xi = 0.01, \omega = 0.1$. Adopted from [61]

2.3 Separation of Bounded Oscillatory Motion from Drift [43]

The investigated system exhibits a non-stationary motion, which means that the displacements of the mass and the slider are unbounded. In addition, the dynamics of this system is very complex ranging from different types of periodic motion to chaos [46]. These facts rise some difficulties in analysing the system dynamics in a standard way. A simple co-ordinates transformation was proposed in [43], which resolved the problem, and it is described below.

We introduce a new system of co-ordinates (p,q,v) instead of (x,z,v):

$$\begin{aligned} p &= x - v, \\ q &= z - v. \end{aligned} \tag{24}$$

The main aim of this transformation is to separate the oscillatory motion of the system from the drift. In the new co-ordinates system, p and q are displacements of the mass and the slider top relative to the current position of the slider bottom v. We will demonstrate that the introduction of the new co-ordinates allows to study a non-stationary motion shown in Fig. 11(a) as independent bounded oscillations depicted in Fig. 11(b) and a dependent on them drift shown in Fig. 11(c).

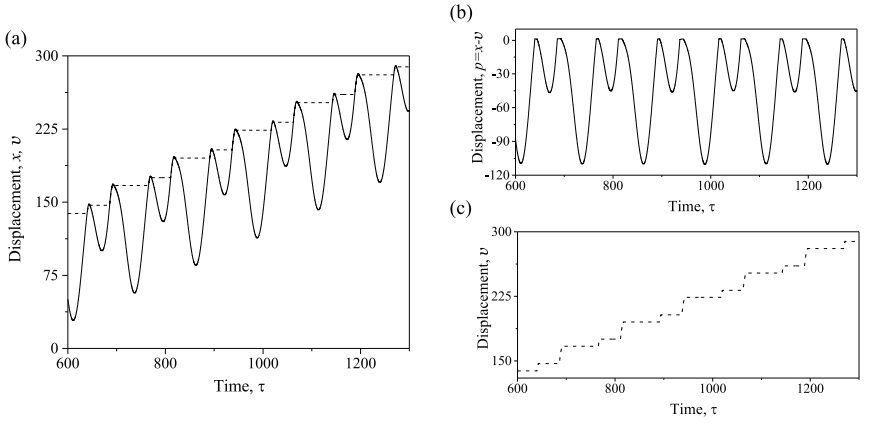

Fig. 11 Time histories of **a** drifting displacement of the mass (solid line) and the slider bottom (dash line); **b** bounded displacement of the mass $p = x - v$; and **c** progressive displacement of the slider bottom v. Adopted from [43]

The equations of motion for each phase can be rewritten as follow:

No contact

$$\begin{aligned} p' &= y, \\ y' &= a\cos(\omega\tau+\varphi)+b, \quad \text{for } p < q+g, \\ q' &= -\frac{1}{2\xi}q, \\ v' &= 0. \end{aligned} \tag{25}$$

Contact without progression

$$\begin{aligned} p' &= y, \\ y' &= -2\xi y - q + a\cos(\omega\tau+\varphi)+b, \quad \text{for } p = q+g \text{ and } 0 < 2\xi y + q < 1, \\ q' &= y, \\ v' &= 0. \end{aligned} \tag{26}$$

Contact with progression

$$\begin{aligned} p' &= -\frac{1}{2\xi}(q-1), \\ y' &= a\cos(\omega\tau+\varphi)+b-1, \quad \text{for } p = q+g \text{ and } 2\xi y + q \geq 1, \\ q' &= -\frac{1}{2\xi}(q-1), \\ v' &= y + \frac{1}{2\xi}(q-1). \end{aligned} \tag{27}$$

As can be seen by closer examination of Eqs. (25), (26) and (27), the first three equations of each set describing the mass and slider top motions do not depend on the displacement of the slider bottom, v. Therefore, there is no influence of the progression v on the bounded system dynamics. On contrary the motion of the slider bottom depends on the mass velocity and the displacement of the slider top (see the last equation of Eqs. (27)), hence the progression (drift) can be determined once the oscillatory mass and the slider top motions are known.

The equations of motion describing bonded oscillations are linear for each phase, and therefore the global solution can be constructed by stitching the local solutions for each phase at the points of discontinuities (non-smoothness) in the same way as it was done for the unbounded system. The set of initial values $(\tau_0; p_0, y_0, q_0)$ defines in which phase the system will operate. If $p_0 < q_0 + g$, it will be *No contact* phase. For $p_0 = q_0 + g$, it will be *Contact without progression* phase if $0 < 2\xi y_0 + q_0 < 1$ or *Contact with progression* phase if $2\xi y_0 + q_0 \geq 1$. When the conditions in the current phase fail, the next phase begins, and the final displacements and velocity for the preceding phase define the initial conditions for the next one.

The progression $v(\tau)$ can be calculated separately if the dynamics of the bounded system (p, y, q) is known (i.e. the sequence of the phases and the initial conditions for them). By solving the forth part of Eqs. (25), (26) and (27), we learnt that during the *No contact* and *Contact without progression* phases the progression does not change its value and is equal to

$$v(\tau) = v_0. \tag{28}$$

The progression during the *Contact with progression* phase can be calculated as

$$v(\tau) = v_0 + p_0 - g - 1 + (p_0 - g - 1)\exp\left(-\frac{\tau - \tau_0}{2\xi}\right) + y_0(\tau - \tau_0) + \frac{b-1}{2}(\tau - \tau_0)^2 - \frac{a}{\omega^2}\left[\cos(\omega\tau + \varphi) - \cos(\omega\tau_0 + \varphi) + \omega(\tau - \tau_0)\sin(\omega\tau_0 + \varphi)\right]. \tag{29}$$

The introduced co-ordinate transformation allows to study dynamics of the systems with drift in the same way as systems exhibiting bounded oscillations. Once the drift is subtracted from the oscillatory motion the standard nonlinear dynamics tools including the cell-to-cell mapping method [26] can be deployed to find co-existing attractors and their basins. For example, an evolution of the strange attractor and co-existing periodic orbits under increasing frequency ω is shown in Fig. 12 for $a = 0.3,\ b = 0.1,\ \xi = 0.1$. The presented basins of attractions were constructed using *Dynamics* software [65] adopting the following colour coding. The strange chaotic attractor and its basin are marked in orange and yellow respectively. The period four motion and its basin are coloured in black and purple. Red colour marks the attractor for blue basin, and green colour marks the attractor for pink basin. All presented cases have fractal boundaries of attractions. As can be seen from Fig. 12 co-existence of two (Fig. 12(a) and 12(d)) and three (Fig. 12(b), 12(c), 12(e) and 12(f)) attractors were found for this set of parameters.

2.4 Conclusions

In this section we presented the study of a drifting oscillator as an effective model for a vibro-impact moling system. The detailed mathematical modelling of the drifting oscillator was presented and the developed model was calibrated by the experiments.

The undertaken nonlinear dynamics analysis suggests the best progression rates are achieved for a period one motion, which means the period of response is equal to the period of excitation. Based on this finding a semi-analytical method to determine the best progression rates was developed. The parametric studies unveiled the best progression can be obtained for: (i) the ratio between the dynamic amplitude and static force around 2 and (ii) low excitation frequencies when compared with the natural frequency of the penetrated media.

To simplify the analysis further, a special coordinate transformation was proposed in order to separate the bounded oscillations of the impacting mass from the drifting motion. This transformation allows to use the standard nonlinear dynamics tools to analyse the dynamics of the bounded motion first and then reconstruct the drift (progression). After applying this transformation, the basins of attractions were calculated for the bounded system, and a number of co-existing solutions were observed for the higher excitation frequency.

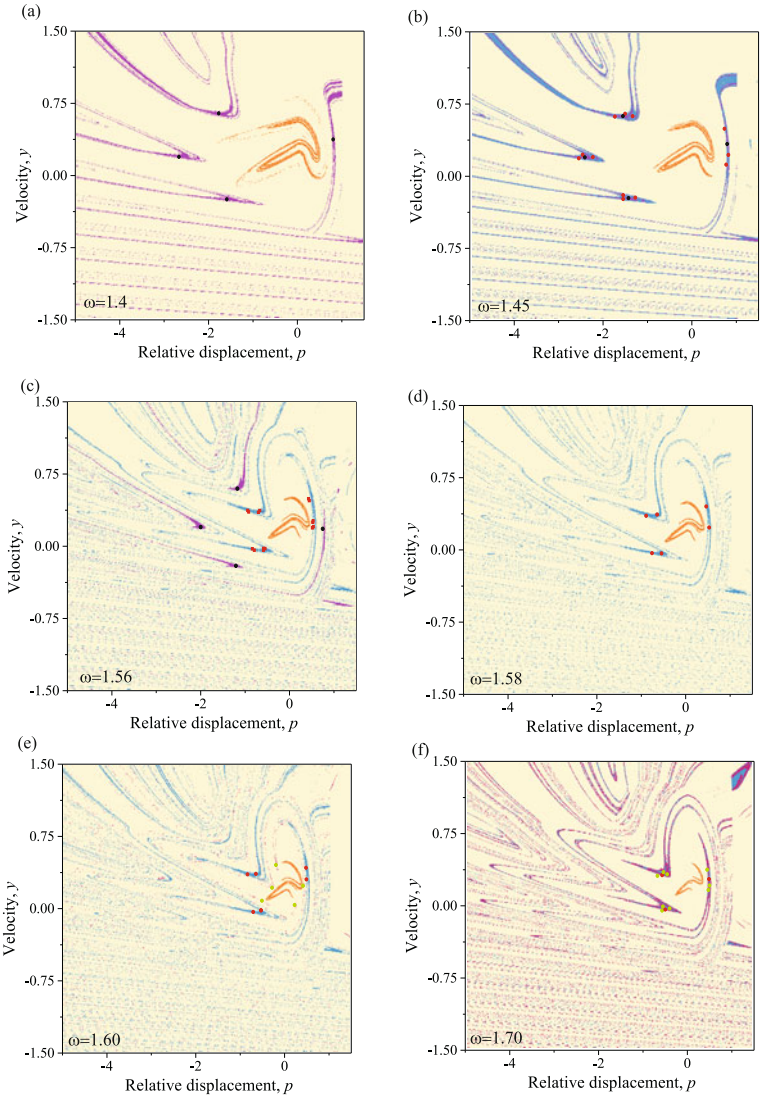

Fig. 12 Evolution of basins of attraction [43] for $a = 0.3,\ b = 0.1,\ \xi = 0.1$; **a** $\omega = 1.4$, **b** $\omega = 1.45$, **c** $\omega = 1.56$, **d** $\omega = 1.58$, **e** $\omega = 1.60$ and **f** $\omega = 1.70$

3 Nonlinear Dynamics Caused by Fatigue Crack Growth [18, 15, 16, 19, 17]

The main aim of this section is to study the effects of fatigue crack growth on the dynamic responses of engineering components and structures [18, 15, 16, 19, 17]. Due to the fact that the dynamic responses of a standard cracked specimen are

often constrained by the kinematics of the forcing mechanisms in the conventional fatigue-testing machines, the natural response of the cracked specimen cannot be easily obtained. Therefore, a novel fatigue-testing rig was designed and built as detailed in [15, 16]. This novel rig consists of two base-excited oscillators, one positioned above and the other below a Single-Edge-Notched Beam (SENB) specimen and being excited by an electro-dynamic shaker. The main operating principle of the rig is that inertial forces generated by the oscillators act on the specimen, in which crack opens and closes. The rig was modelled mathematically as a two mass and one mass system, and the non-smoothness in these systems comes from the opening and closing of a fatigue crack.

3.1 Fatigue-Testing Rig and Experimental Set-Up [16, 19]

The fatigue-testing rig as shown in Fig. 13 consists of two base-excited oscillators, which are positioned above and below a SENB specimen. Each mass sandwiches a pair of leaf springs, which are also sandwiched and bolted on tower 1. These two

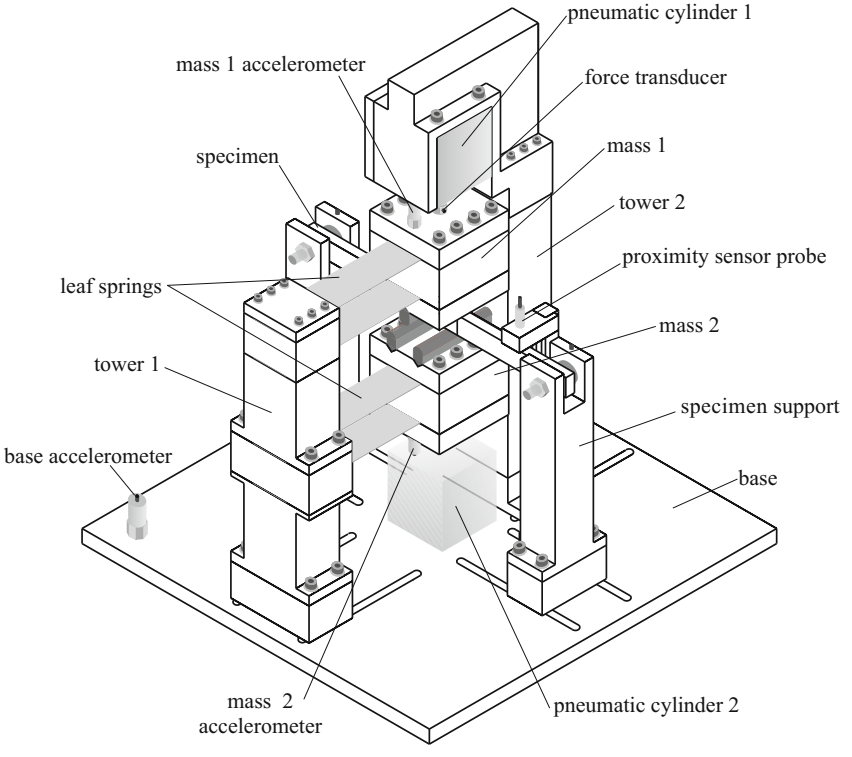

Fig. 13 Fatigue-testing rig [19] developed at the Centre for Applied Dynamics Research of the University of Aberdeen

pairs of leaf springs prevent the masses from rotating during oscillations, hence, the line of action of the applied force is perpendicular to the neutral axis of the specimen. The stiffness of the leaf springs can be adjusted by sliding tower 1 along the slot on the base. The specimen is held by supports at both ends, which are adjustable (by sliding along the slot on the base) to accommodate a range of specimen lengths. The specimen is then in turn held in place on the supports by a means of loading pins.

During experiments, both oscillators are kept in contact with the specimen by the aid of the pre-loads from the pneumatic cylinders. In addition, the pneumatic cylinders are used to set the prescribed mean load on the specimen by appropriately adjusted pressures at the top and the bottom. With this loading arrangement fatigue testing of positive (tension), negative (compression) or zero mean stresses can be carried out.

The test rig has been mounted on an electro-dynamic shaker which provides the base excitation causing the inertial forces of both oscillators to be generated and to act on the specimen. During the downward motion, the inertia of mass 1 exerts a load on the specimen causing the crack to open and the inertia of mass 2 is responsible for closing the crack during the upward motion. The amount of inertial force induced on a specimen is controlled by the adjustment of amplitude and frequency of the base excitation. The excitation waveform used to drive the shaker can be periodic or aperiodic (quasi periodic, chaotic or stochastic).

In the present studies, samples were made out of aluminium alloy 2024-T351 with the mechanical properties and chemical composition given in Tables 1 and 2, respectively. For all experiments, the same sample type, SENB, was used as shown in Fig. 14 having a width and thickness of $W = 20$mm and $B = 10$mm, respectively. The size of the notch was 5mm long and 1.5mm wide, and the loading span was 270mm.

The rig was mounted on the electro-dynamic shaker, and the base excitation was controlled by the data acquisition unit using *Labview*. The accelerations of the base ($\ddot{x}_b$), mass 1 ($\ddot{x}_{m_1}$), and mass 2 ($\ddot{x}_{m_2}$), were measured by calibrated accelerometers. A

Table 1 Material properties for aluminium alloy 2024-T351 [19]

Property	Value
Tensile strength	454MPa
Yield strength	317MPa
Young's modulus	72.4GPa
Density	2780kg/m^3

Table 2 Chemical composition for aluminium alloy 2024-T351 [19]

AL	Si	Fe	Cu	Mn	Mg	Cr	Zn	Ti
93.63	0.09	0.21	4.06	0.47	1.37	0.01	0.14	0.02

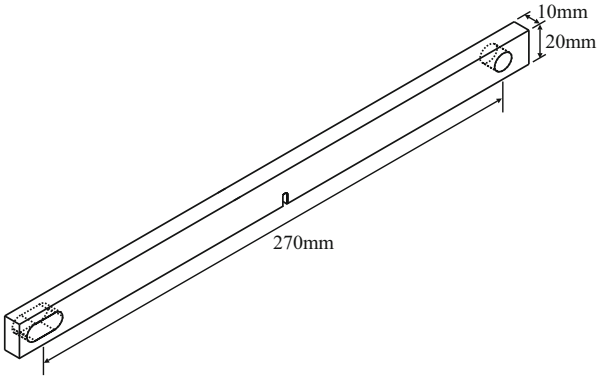

Fig. 14 Geometry of a Single-Edge-Notched Beam (SENB) specimen [19]

signal from each accelerometer and an output of each force transducer (f_{c_1} and f_{c_2}) were passed through a charge amplifier and monitored on an oscilloscope before being captured on the data acquisition unit. A schematic of the measurement block diagram is shown in Fig. 15.

The signal of the proximity sensor which represents the relative displacement (z_s) between the specimen and the base was passed through a 1kHz low pass filter to remove the high frequency noise. The output of the low pass filter was then connected to a power supply before being registered on the data acquisition unit. Finally, the signal from the ACPD crack growth monitor was fed to the data acquisition unit via a power amplifier and an oscilloscope.

In addition to measuring the relative displacement between the test specimen and the base, the proximity sensor was also used to set the dynamic load amplitude of the specimen. For these reasons, the proximity sensor was calibrated to obtain the displacement versus the sensor output voltage and the load versus the sensor output voltage relationships. During the calibration procedure the central position of the specimen was displaced by a known distance and, at each increment, the output voltage of the proximity sensor was recorded.

To complete the calibration procedure, the compliance of the cracked specimen was evaluated. The total compliance, C_{tot}, as a function of crack length of a through-thickness cracked beam can be calculated as [3]

$$C_{tot} = C_{nc} + C_c, \tag{30}$$

where C_{nc} is the compliance in the absence of a crack and C_c is the additional compliance due to the crack. For the case of a three-point loaded crack-free beam, the compliance, C_{nc}, is given as,

$$C_{nc} = \frac{L_{span}^3}{48EI}, \tag{31}$$

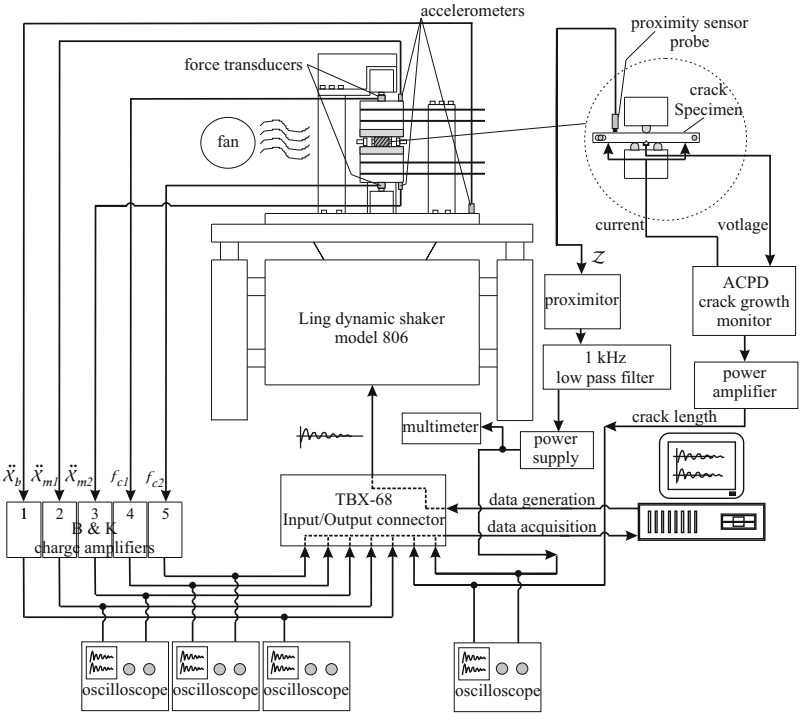

Fig. 15 Experimental layout of the fatigue-testing device for inducing dynamic loading [19]

where L_{span} is the loading span, E is Young's modulus, I is the second moment of area $\left(BW^3/12\right)$, B is the thickness and W is the width of the beam. The compliance, C_c, of the three-point loaded SENB for any value of span-to-width ratio (e.g. $\beta = L_{span}/W$) larger than 2.5 has been developed by Guinea *et al.* [25] in the following form

$$C_c = \frac{c_1(\alpha) + \beta c_2(\alpha) + \beta^2 c_3(\alpha)}{EB}, \tag{32}$$

where

$$c_1(\alpha) = -0.378\alpha^3 \ln(1-\alpha) + \alpha^2 \frac{0.29 + 1.39\alpha - 1.6\alpha^2}{1 + 0.54\alpha - 0.84\alpha^2},$$

$$c_2(\alpha) = 1.1\alpha^3 \ln(1-\alpha) + \alpha^2 \frac{-3.22 - 16.4\alpha + 28.1\alpha^2 - 11.4\alpha^3}{(1-\alpha)(1 + 4.7\alpha - 4\alpha^2)},$$

$$c_3(\alpha) = -0.176\alpha^3 \ln(1-\alpha) + \alpha^2 \frac{8.91 - 4.88\alpha - 0.435\alpha^2 + 0.26\alpha^3}{(1-\alpha)^2(1 + 2.9\alpha)},$$

$\alpha = a/W$ is the crack ratio and a is the crack length. Substituting Eqs. (31) and (32) into Eq. (30), and rearranging, the load versus sensor output voltage relationship as a function of crack ratio is obtained:

$$P = \frac{\dfrac{G_f}{1000} \times V_{so}}{\dfrac{L_{span}^3}{48EI} + \dfrac{c_1(\alpha) + \beta c_2(\alpha) + \beta^2 c_3(\alpha)}{EB}}, \tag{33}$$

where G_f is the gain factor (displacement versus sensor output voltage relationship as obtained from above), V_{so} is the sensor output voltage and P is the load. It is worth noting that $\dfrac{G_f}{1000} \times V_{so}$ represents the deflection of the specimen.

A typical test was conducted in the following manner. Before a specimen was pre-loaded, an initial value of the proximity sensor was offset to zero. The amplitude of the proximity sensor output voltage corresponding to the load amplitudes acting on the bending specimen was calculated using Eq. (33). The excitation frequency was set to a value of interest and the base amplitude was varied gradually until the amplitude of the output voltage from the proximity sensor coincided with the calculated value.

3.2 Experimental Results [16]

To investigate the interactions between vibrations and crack growth by experimental means an extensive experimental fatigue test programme was conducted. Fatigue tests were carried out on SENB specimen shown in Fig. 14 and described earlier.

An example result of the measured time histories with the dynamic shaker driven by a sinusoidal waveform is shown in Fig. 16, where the base acceleration (Fig. 16(a)), absolute acceleration of mass 1 (Fig. 16(b)), relative displacement of the SENB specimen (Fig. 16(c)) and dynamic force between pneumatic cylinder 1 and mass 1 (Fig. 16(d)) are presented. For this particular test, the sample was subjected to a mean load of 100N and an amplitude of 100N. Examining time histories of Figs. 16(b) and 16(c), it is evident that the existence of a growing fatigue crack affects the dynamic response of the system, by breaking the symmetry of both acceleration and displacement with respect to their equilibrium positions. Fig. 17 shows the experimental time histories with the shaker driven by a chaotic waveform. The chaotic signal was obtained from the response of a forced Duffing oscillator. The test sample was subjected to zero mean load, in which the fatigue crack was opened and closed (depending on the phase of oscillations) during vibrations. A close scrutiny of the time histories (Fig. 17) shows that the pattern of the responses (Fig. 17(b)) are very similar to the base excitation (Fig. 17(a)).

The load parameters given in Table 3 were selected to compare the fatigue life of the specimen for the effects of mean load and load amplitude under constant amplitude loading.

The excitation frequency of all tests was fixed at 20Hz. Since in our tests aperiodic loading will be used (e.g. Fig. 17), instead of having a typical abscissa of

Table 3 Loading parameters for harmonic excitation fatigue test

Test name	Mean load (N)	Load amplitude (N)	R ratio	Time to fracture (secs)
hl0(78.5)	0	78.5	-1	39801
hl0(100)	0	100	-1	9191
hl0(273.5)	0	273.5	-1	1319
hl100(100)	100	100	0	1628
hl150(50)	150	50	0.5	2288
hl150(100)	150	100	0.2	547
hl200(50)	200	50	0.6	2037
hl200(100)	200	100	0.33	331

number of cycles, excitation time was used. The crack growth curves for the effect of mean load are depicted in Fig. 18, and for the effect of load amplitude are shown in Figs 19 and 20.

For the same load amplitude of 100N on each curve (Fig. 18), the fatigue life decreases as the mean load increases. In Fig. 19, when the load amplitude increases

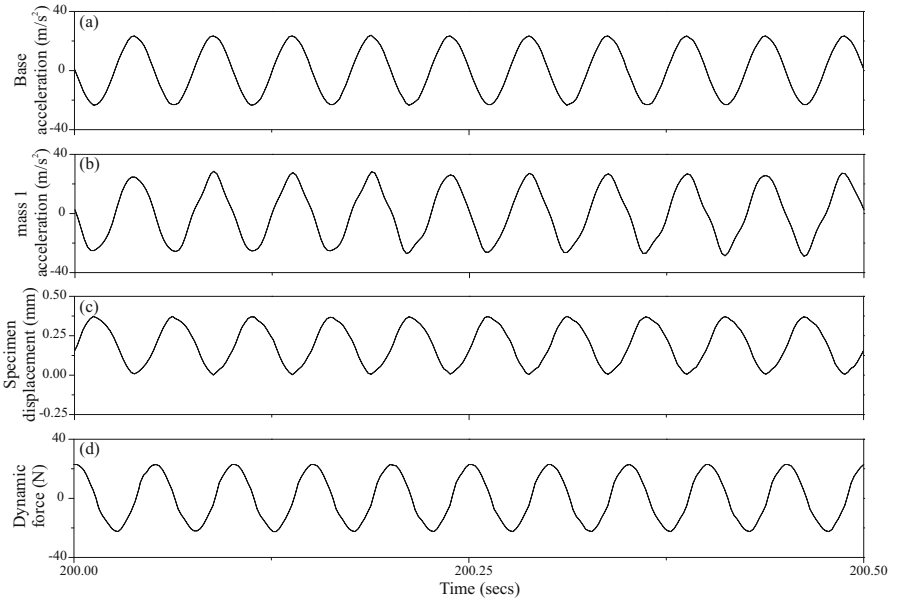

Fig. 16 Time histories [16] under harmonic excitation: (a) base acceleration, (b) mass 1 acceleration, (c) specimen displacement and (d) dynamic force between pneumatic cylinder 1 and mass 1.

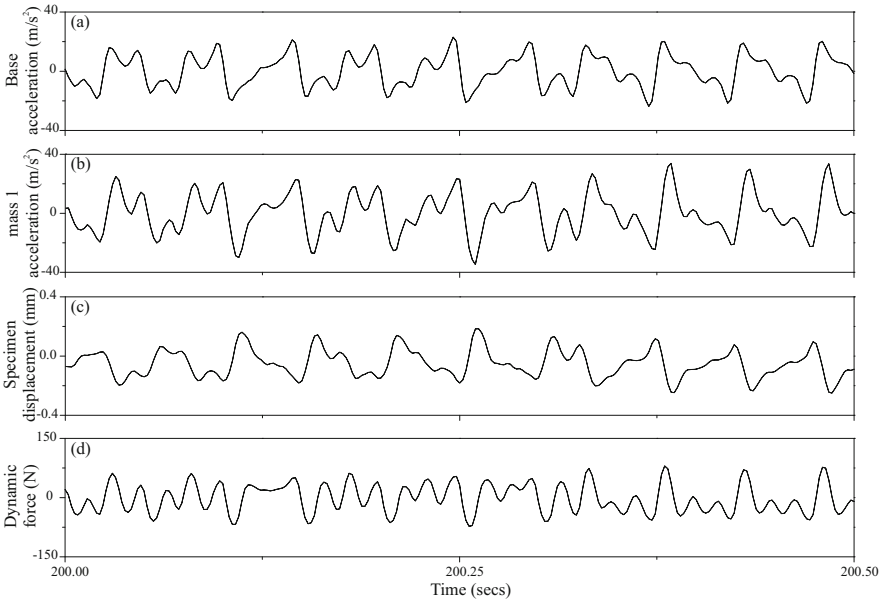

Fig. 17 Time histories [16] under chaotic excitation: **a** base acceleration, **b** mass 1 acceleration, **c** specimen displacement and **d** dynamic force between pneumatic cylinder 1 and mass 1

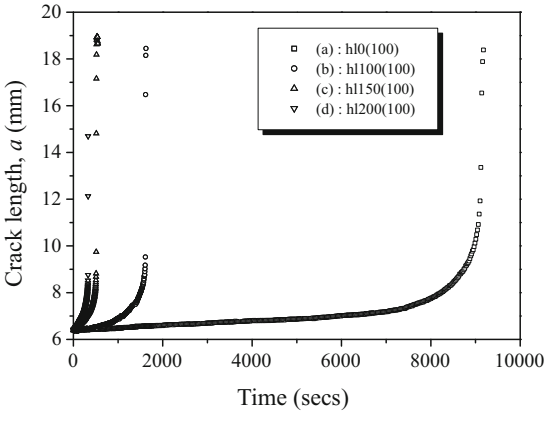

Fig. 18 Fatigue crack length [16] versus time for fixed load amplitude of 100N and with mean load of (a) 0N, (b) 100N, (c) 150N and (d) 200N

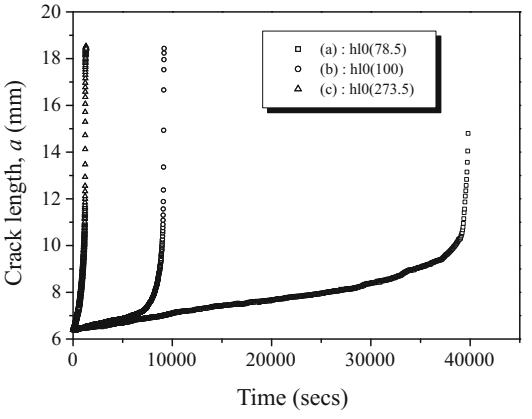

Fig. 19 Fatigue crack length [16] versus time for fixed mean load of 0N and with load amplitude of (a) 78.5N, (b) 100N and (c) 273.5N

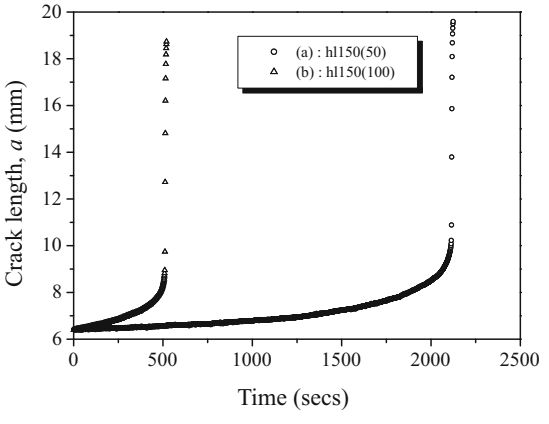

Fig. 20 Fatigue crack length [16] versus time: fixed mean load of 150N for load amplitude of (a) 50N and (b) 100N

the fatigue life decreases for the same mean load of 0N applied on each curve. A similar trend can be found for a fixed mean load of 150N in Fig. 20. The time to fracture starting from a pre-cracked length of 6.4mm for each test are given in the last column of Table 3. Time to fracture is longer for test hl150(50), which has a lower load amplitude but a higher mean load when compared to test hl100(100) (in which both tests have identical maximum load of 200N). A similar trend has been found for tests hl150(100) and hl200(50) where both tests have the same maximum load of 250N. Hence, it is not sensible to compare fatigue life by the maximum load, but rather by the mean load and load amplitude.

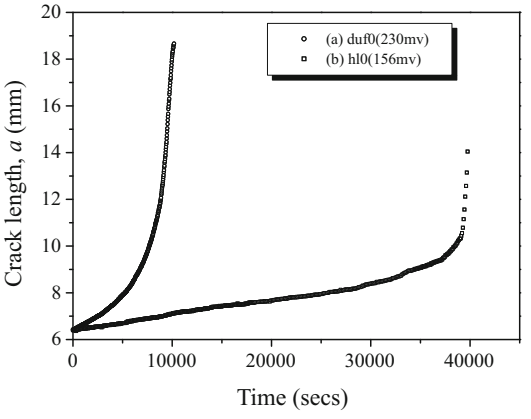

Fig. 21 Fatigue crack length [16] versus time for mean load of 0N: (a) Duffing excitation and (b) harmonic excitation

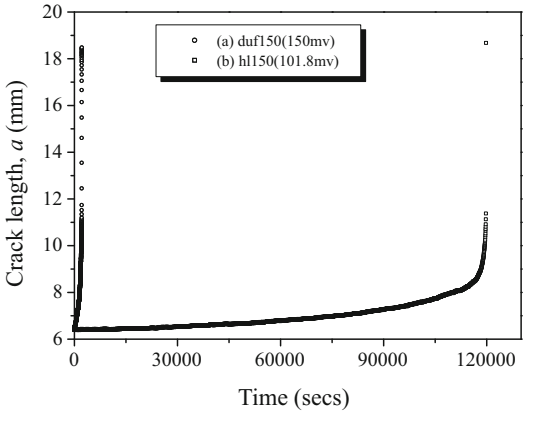

Fig. 22 Fatigue crack length [16] versus time for mean load of 150N: (a) Duffing excitation and (b) harmonic excitation

The fatigue life of SENB specimen is compared between harmonic and chaotic excitations for the same amount of elastic energy generated in the specimen. Practically, an equal amount of power was used to drive the dynamic shaker for both excitations (harmonic and chaotic). The dominant frequency for the Duffing wave is 20Hz (an example of the Duffing wave is shown in Fig. 17(a)). The excitation frequency for harmonic wave is also 20Hz. Figs 21 and 22 show the crack growth curves for the specimen subjected to mean load of 0N and 150N, respectively. On both figures, the crack curves for harmonic loading are plotted using squares and for chaotic loading uses circles. Referring to Fig. 21, for the same amount of energy the time to fracture for harmonic excitation requires 4 times more than chaotic

excitation. A similar trend can be seen in Fig. 22 when the specimen is subjected to a mean load of 150N, where the fatigue life of the specimen under harmonic excitation is 56 times longer than chaotic excitation. These results indicate that for the same amount of energy pumped in into a specimen chaotic excitation is much more damaging than harmonic. The main reason for a much shorter fatigue life with specimen undergoing chaotic excitation is that the loading contains high frequency oscillations (see Fig. 17a).

3.3 Two Mass Model [18, 19]

The experimental rig shown in Fig. 13 can be described by a physical model depicted in Fig. 23, where the mass m_1 is attached to two springs and two dashpot dampers, in which k_{Ls1} and c_{Ls1} represent stiffness and damping of the top leaf spring, respectively, and k_{p1} and c_{p1} are stiffness and damping of the top pneumatic cylinder. The mass m_2 is attached to the base in the same way as mass m_1. Here, k_{Ls2} and c_{Ls2} represent the stiffness and damping of the bottom leaf spring, k_{p2} and c_{p2} are the stiffness and damping of the bottom pneumatic cylinder. All springs are assumed to be linear and the dampers are assumed to be linearly viscous. Masses of all springs and dampers are neglected. To ensure that both masses are kept in contact with the specimen during operation, the pneumatic forces P_1 and P_2 act on masses m_1 and m_2, respectively. The system is excited harmonically from the base with amplitude A_b and frequency Ω.

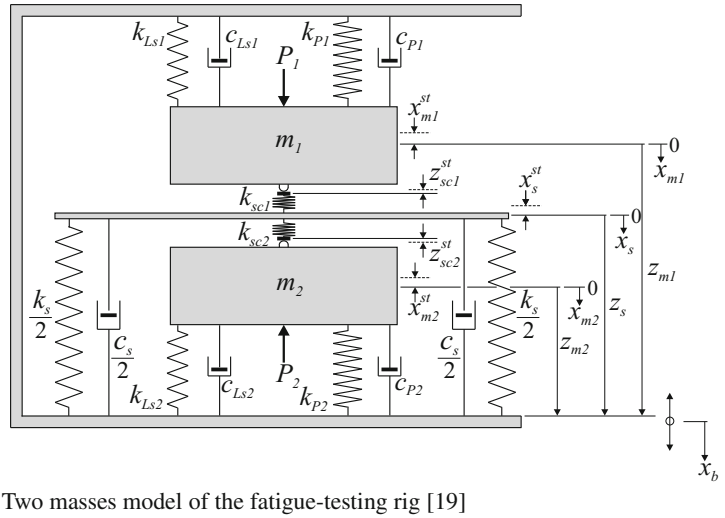

Fig. 23 Two masses model of the fatigue-testing rig [19]

Due to the fact that the operating frequency range is much lower than the fundamental frequency of the crack-free specimen, its inertial effects affecting the dynamics of the entire rig are considered to be negligible. As a consequence, the crack-free

sample is modelled as a discrete linear spring k_s with a viscous damping coefficient c_s. As can be seen in Fig. 23, the model of the specimen comprises of a rigid massless beam attached to two massless springs of $0.5k_s$ stiffness each together with two massless dashpot dampers of $0.5c_s$ viscous damping each.

Elastic deformations at the point of contacts between the pneumatic cylinders and the surface of the specimen were assumed. The introduced contact stiffnesses k_{sc1} and k_{sc2} as shown in Fig. 23, are much larger than the stiffness of the specimen k_s. These springs are needed to determine the change from *Contact* and *No contact* phases.

Due to the pneumatic forces (P_1 and P_2) and also the gravitational forces ($m_1 g$ and $m_2 g$), the specimen is loaded from the top and the bottom by $k_{sc1} z_{sc1}^{st}$ and $-k_{sc2} z_{sc2}^{st}$, respectively, where

$$z_{sc1}^{st} = x_{m1}^{st} - x_s^{st}, \quad z_{sc2}^{st} = x_{m2}^{st} - x_s^{st}$$

and, x_{m1}^{st}, x_{m2}^{st} and x_s^{st} are the static displacements of masses m_1, m_2 and the specimen, respectively.

Depending on the pre-loading forces ($P_1 + m_1 g$ and $-P_2 + m_2 g$), the fatigue rig may operate in one of the following phases: (i) Full contact of both masses with the specimen, (ii) Partial contact where the mass m_1 lost contact while the mass m_2 is in contact with the specimen, (iii) Partial contact where the mass m_2 lost contact while the mass m_1 is in contact with the specimen, and finally (iv) No contact where both masses lost contact with the specimen. When both masses are in contact with the specimen (Phase (i)), the relative displacements of the masses, z_{m1} and z_{m2}, and the specimen, z_s, are oscillating in phase. In addition, if k_{sc1} and k_{sc2} are equal and also if the springs and the dampers that are attached to mass m_1 are identical to those on m_2, then for the considered system the displacements of masses m_1 and m_2 are equal, $z_{m1} = z_{m2}$. For Phase (i) the equations of motion are

$$\begin{aligned}
&m_1 \ddot{z}_{m1} + (c_{Ls1} + c_{p1})\dot{z}_{m1} + (k_{Ls1} + k_{p1} + k_{sc1}) z_{m1} - k_{sc1} z_s = m_1 A_b \Omega^2 \sin(\Omega t),\\
&c_s \dot{z}_s + (k_s + k_{sc1} + k_{sc2}) z_s - k_{sc1} z_{m1} - k_{sc2} z_{m2} = 0,\\
&m_2 \ddot{z}_{m2} + (c_{Ls2} + c_{p2})\dot{z}_{m2} + (k_{Ls2} + k_{p2} + k_{sc2}) z_{m2} - k_{sc2} z_s = m_2 A_b \Omega^2 \sin(\Omega t).
\end{aligned} \tag{34}$$

For Phase (ii) to occur, the following inequality $z_{m1} < (z_s - z_{sc1}^{st})$, has to be satisfied and the force acting between m_1 and the specimen needs to vanish; $k_{sc1}(z_{m1} - z_s + z_{sc1}^{st}) = 0$. Hence the equations of motion are as follows

$$\begin{aligned}
&m_1 \ddot{z}_{m1} + (c_{Ls1} + c_{p1})\dot{z}_{m1} + (k_{Ls1} + k_{p1}) z_{m1} + k_{Ls1} x_{m1}^{st} = P_1 + m_1 g \\
&\qquad\qquad + m_1 A_b \Omega^2 \sin(\Omega t),\\
&c_s \dot{z}_s + (k_s + k_{sc2}) z_s - k_{sc2} z_{m2} + k_s x_s^{st} - k_{sc2} z_{sc2}^{st} = 0,\\
&m_2 \ddot{z}_{m2} + (c_{Ls2} + c_{p2})\dot{z}_{m2} + (k_{Ls2} + k_{p2} + k_{sc2}) z_{m2} - k_{sc2} z_s = m_2 A_b \Omega^2 \sin(\Omega t).
\end{aligned} \tag{35}$$

For Phase (iii) to occur, $z_{m2} > (z_s - z_{sc2}^{st})$ has to be satisfied and the forces acting between m_2 and the specimen needs to vanish; $k_{sc2}(z_{m2} - z_s + z_{sc2}^{st}) = 0$. The equations of motion are

$$m_1\ddot{z}_{m1} + (c_{Ls1} + c_{p1})\dot{z}_{m1} + (k_{Ls1} + k_{p1} + k_{sc1})z_{m1} - k_{sc1}z_s = m_1A_b\Omega^2\sin(\Omega t),$$

$$c_s\dot{z}_s + (k_s + k_{sc1})z_s - k_{sc1}z_{m1} + k_s x_s^{st} - k_{sc1}z_{sc1}^{st} = 0, \tag{36}$$

$$m_2\ddot{z}_{m2} + (c_{Ls2} + c_{p2})\dot{z}_{m2} + (k_{Ls2} + k_{p2})z_{m2} + k_{Ls2}x_{m2}^{st} = -P_2 + m_2g + m_2A_b\Omega^2\sin(\Omega t).$$

Finally, for Phase (iv) to occur, $z_{m1} < (z_s - z_{sc1}^{st})$ and $z_{m2} > (z_s - z_{sc2}^{st})$ have to be satisfied simultaneously. The equations of motion are

$$\begin{aligned} m_1\ddot{z}_{m1} + (c_{Ls1} + c_{p1})\dot{z}_{m1} + (k_{Ls1} + k_{p1})z_{m1} + k_{Ls1}x_{m1}^{st} &= P_1 + m_1g \\ &\quad + m_1A_b\Omega^2\sin(\Omega t), \\ c_s\dot{z}_s + k_s z_s + k_s x_s^{st} &= 0, \end{aligned} \tag{37}$$

$$m_2\ddot{z}_{m2} + (c_{Ls2} + c_{p2})\dot{z}_{m2} + (k_{Ls2} + k_{p2})z_{m2} + k_{Ls2}x_{m2}^{st} = -P_2 + m_2g + m_2A_b\Omega^2\sin(\Omega t).$$

The following simplifying assumptions were made

$$m_1 \approx m_2 = m,\ \ c_{Ls1} \approx c_{Ls2} = c_{Ls},\ \ k_{Ls1} \approx k_{Ls2} = k_{Ls},\ \ k_{sc1} \approx k_{sc2} = k_{sc}.$$

The equations of motion, Eqs. (34)-(37), are now non-dimensionalised by introducing the following non-dimensional variables

$$\tau = \omega_{Ls}t,\ \ X_1 = \frac{z_{m1}}{A_b},\ \ X_2 = X_1' = \frac{\dot{z_{m1}}}{A_b\omega_{Ls}},\ \ X_3 = \frac{z_s}{A_b},\ \ X_4 = \frac{z_{m2}}{A_b},$$

$$X_5 = X_4' = \frac{\dot{z_{m2}}}{A_b\omega_{Ls}},\ \ X_b = \frac{x_b}{A_b} = \sin(\eta_{Ls}\tau),$$

and parameters

$$\omega_{Ls} = \sqrt{\frac{k_{Ls}}{m}},\ \ \xi_{Ls} = \frac{c_{Ls}}{2m\omega_{Ls}},\ \ \omega_s = \sqrt{\frac{k_s}{m}},\ \ \xi_s = \frac{c_s}{2m\omega_s},\ \ \omega_{p1} = \sqrt{\frac{k_{p1}}{m}},$$

$$\xi_{p1} = \frac{c_{p1}}{2m\omega_{p1}},\ \ \omega_{p2} = \sqrt{\frac{k_{p2}}{m}},\ \ \xi_{p2} = \frac{c_{p2}}{2m\omega_{p2}},\ \ \lambda_1 = \sqrt{\frac{k_{p1}}{k_{Ls}}},\ \ \lambda_2 = \sqrt{\frac{k_{p2}}{k_{Ls}}},$$

$$\vartheta = \sqrt{\frac{k_s}{k_{Ls}}},\ \ \varepsilon = \frac{k_{Ls}}{k_{sc}},\ \ \delta_1 = \frac{x_{m1}^{st}}{A_b},\ \ \delta_2 = \frac{x_{m2}^{st}}{A_b},\ \ \Delta_1 = \frac{z_{sc1}^{st}}{A_b},\ \ \Delta_2 = \frac{z_{sc2}^{st}}{A_b},$$

$$\gamma_s = \frac{x_s^{st}}{A_b}, \quad \eta_{Ls} = \frac{\Omega}{\omega_{Ls}}, \quad f_1 = \frac{P_1 + mg}{mA_b\omega_{Ls}^2}, \quad f_2 = \frac{P_2 - mg}{mA_b\omega_{Ls}^2},$$

where $'$ denotes $d/d\tau$.

Eqs. (34) to (37) are transformed to a set of the first order differential equations which can be written for each phase as

Phase (i)

$$\begin{aligned}
X_1' &= X_2,\\
X_2' &= -\left(1+\lambda_1^2+\frac{1}{\varepsilon}\right)X_1 - (2\xi_{Ls}+2\xi_{p1}\lambda_1)X_2 + \frac{1}{\varepsilon}X_3 + \eta_{Ls}^2\sin(\eta_{Ls}\tau),\\
X_3' &= \frac{1}{2\varepsilon\vartheta\xi_s}X_1 - \left(\frac{1}{\varepsilon\vartheta\xi_s}+\frac{\vartheta}{2\xi_s}\right)X_3 + \frac{1}{2\varepsilon\vartheta\xi_s}X_4,\\
X_4' &= X_5,\\
X_5' &= \frac{1}{\varepsilon}X_3 - \left(1+\lambda_2^2+\frac{1}{\varepsilon}\right)X_4 - (2\xi_{Ls}+2\xi_{p2}\lambda_2)X_5 + \eta_{Ls}^2\sin(\eta_{Ls}\tau).
\end{aligned} \tag{38}$$

Phase (ii)

$$\begin{aligned}
X_1' &= X_2,\\
X_2' &= -(1+\lambda_1^2)X_1 - (2\xi_{Ls}+2\xi_{p1}\lambda_1)X_2 - \delta_1 + f_1 + \eta_{Ls}^2\sin(\eta_{Ls}\tau),\\
X_3' &= -\left(\frac{1}{2\varepsilon\vartheta\xi_s}+\frac{\vartheta}{2\xi_s}\right)X_3 + \frac{1}{2\varepsilon\vartheta\xi_s}X_4 + \frac{\Delta_2}{2\varepsilon\vartheta\xi_s} - \frac{\vartheta\gamma_s}{2\xi_s},\\
X_4' &= X_5,\\
X_5' &= \frac{1}{\varepsilon}X_3 - \left(1+\lambda_2^2+\frac{1}{\varepsilon}\right)X_4 - (2\xi_{Ls}+2\xi_{p2}\lambda_2)X_5 + \eta_{Ls}^2\sin(\eta_{Ls}\tau).
\end{aligned} \tag{39}$$

Phase (iii)

$$\begin{aligned}
X_1' &= X_2,\\
X_2' &= -\left(1+\lambda_1^2+\frac{1}{\varepsilon}\right)X_1 - (2\xi_{Ls}+2\xi_{p1}\lambda_1)X_2 + \frac{1}{\varepsilon}X_3 + \eta_{Ls}^2\sin(\eta_{Ls}\tau),\\
X_3' &= \frac{1}{2\varepsilon\vartheta\xi_s}X_1 - \left(\frac{1}{2\varepsilon\vartheta\xi_s}+\frac{\vartheta}{2\xi_s}\right)X_3 + \frac{\Delta_1}{2\varepsilon\vartheta\xi_s} - \frac{\vartheta\gamma_s}{2\xi_s},\\
X_4' &= X_5,\\
X_5' &= -(1+\lambda_2^2)X_4 - (2\xi_{Ls}+2\xi_{p2}\lambda_2)X_5 - \delta_2 - f_2 + \eta_{Ls}^2\sin(\eta_{Ls}\tau).
\end{aligned} \tag{40}$$

Phase (iv)

$$
\begin{aligned}
X_1^{'} &= X_2,\\
X_2^{'} &= -(1+\lambda_1^2)X_1 - (2\xi_{Ls}+2\xi_{p1}\lambda_1)X_2 - \delta_1 + f_1 + \eta_{Ls}^2\sin(\eta_{Ls}\tau),\\
X_3^{'} &= -\frac{\vartheta}{2\xi_s}X_3 - \frac{\vartheta\gamma_s}{2\xi_s},\\
X_4^{'} &= X_5,\\
X_5^{'} &= -(1+\lambda_2^2)X_4 - (2\xi_{Ls}+2\xi_{p2}\lambda_2)X_5 - \delta_2 - f_2 + \eta_{Ls}^2\sin(\eta_{Ls}\tau).
\end{aligned}
\tag{41}
$$

To obtain a more elegant and compact formulation, we used the Heaviside step functions to describe the piecewise linear nature of the considered system by defining a set of switch functions G_3 and G_4,

$$
\begin{aligned}
G_3 &= G_3(X_1, X_3) = H(X_1 - (X_3 - \Delta_1)),\\
G_4 &= G_4(X_3, X_4) = H(-X_4 + (X_3 - \Delta_2)).
\end{aligned}
\tag{42}
$$

In Eq. (42), when m_1 loses contact with the specimen, $X_1 < (X_3 - \Delta_1)$, the function G_3 is equal to 0. When m_2 loses contact with the specimen, $X_4 > (X_3 - \Delta_2)$, the function G_4 is equal to 0, otherwise G_3 and G_4 are equal to 1. The equations of motion that describe all the possible phases are:

$$
\begin{aligned}
X_1^{'} &= X_2,\\
X_2^{'} &= -(1+\lambda_1^2)X_1 - (2\xi_{Ls}+2\xi_{p1}\lambda_1)X_2 - \frac{G_3}{\varepsilon}(X_1 - X_3 + \Delta_1) - \delta_1 + f_1\\
&\quad + \eta_{Ls}^2\sin(\eta_{Ls}\tau),\\
X_3^{'} &= \frac{G_3}{2\varepsilon\vartheta\xi_s}(X_1 - X_3 + \Delta_1) + \frac{G_4}{2\varepsilon\vartheta\xi_s}(-X_3 + X_4 + \Delta_2)\\
&\quad - \frac{\vartheta}{2\xi_s}X_3 - \frac{\vartheta\gamma_s}{2\xi_s},\\
X_4^{'} &= X_5,\\
X_5^{'} &= -(1+\lambda_2^2)X_4 - (2\xi_{Ls}+2\xi_{p2}\lambda_2)X_5 - \frac{G_4}{\varepsilon}(-X_3 + X_4 + \Delta_2) - \delta_2 - f_2\\
&\quad + \eta_{Ls}^2\sin(\eta_{Ls}\tau).
\end{aligned}
\tag{43}
$$

Equation (43) was used to compute the dynamic responses including the one shown in Fig. 24 where four phases of motion can be clearly observed for the system with a specimen without a crack. The displacements of mass 1, X_1, and mass 2, X_4, are plotted by thick solid and dashed lines, respectively. The displacement of the specimen, X_3, is plotted in dotted line.

Referring to Fig. 24(b), at the instant when m_1 hits m_2 both masses are kept in contact with the specimen for a very short time (labelled as Phase(i)). After this short period of light impact, due to the energy transfer between m_1 and m_2, m_2 starts to separate while m_1 still follows the trajectory of the specimen (labelled as Phase (iii)).

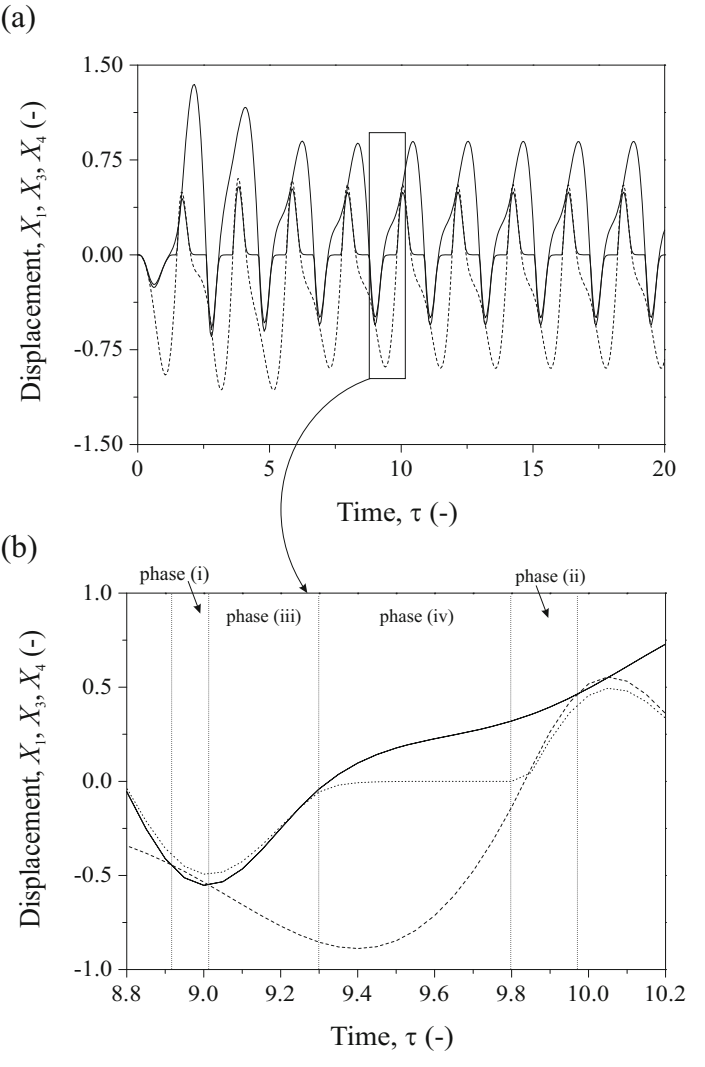

Fig. 24 Time histories [19] computed for $\eta_{Ls} = 3$, $\xi_{Ls} = 0.00255$, $\xi_s = 0.002$, $\xi_{p1} = 0.4$, $\xi_{p2} = 0.4$, $\lambda_1 = 2$, $\lambda_2 = 2$, $\vartheta = 7.828$, $\varepsilon = 0.002012$, $f_1 = 3.75$, $f_2 = 3.75$. Thick solid line represents X_1, dotted line represents X_3 and dash line represents X_4

When m_1 moves upwards to the vicinity of the equilibrium point, Phase (iv) begins. In this phase, the displacement of the specimen decays and remains stationary as at the equilibrium position. When the position of m_2 coincides with the position of the specimen Phase (ii) occurs, in which m_2 moves in phase with the specimen while m_1 is still away from the specimen.

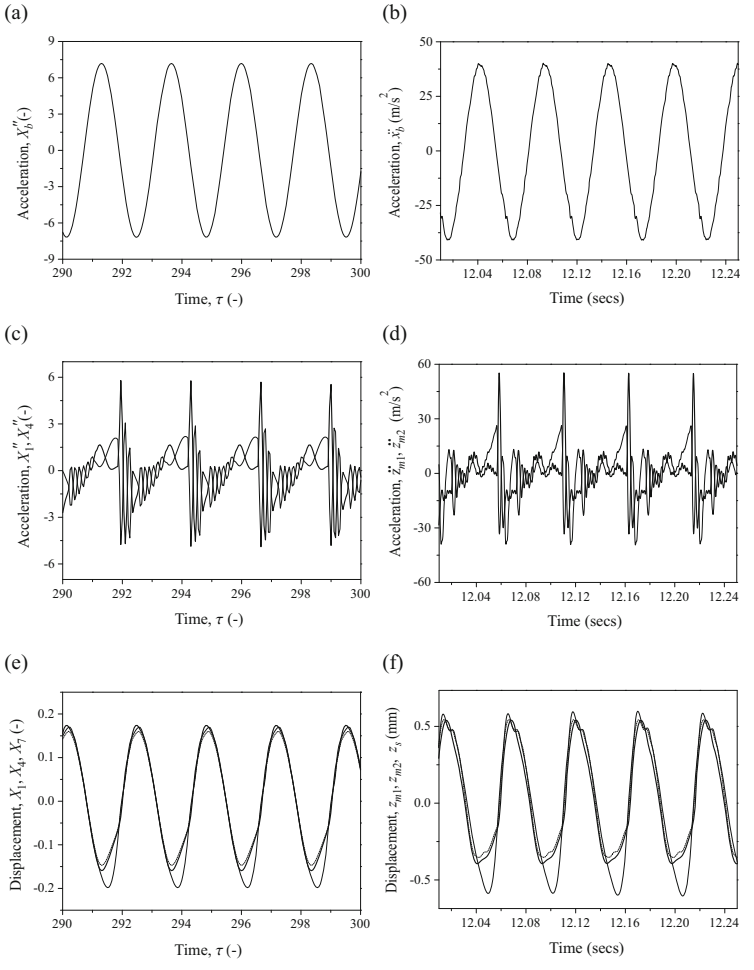

Fig. 25 **a**, **c**, **e** Theoretical time histories for $\eta_{Ls} = 2.5$, $\xi_{Ls} = 0.00255$, $\xi_s = 0.002$, $\xi_{p1} = 0.4$, $\xi_{p2} = 0.4$, $\lambda_1 = 4.36$, $\lambda_2 = 4.36$, $\vartheta = 7.828$, $\varepsilon = 0.002012$, $f_1 = 5.44$, $f_2 = 3.52$; **b**, **d**, **f** Experimental time histories for excitation frequency of 19.15Hz and an amplitude of 2.8mm. Thick solid line represents X_1'', $\ddot{z}_{m1}$, X_1 and z_{m1} and thin solid line represents X_4'', $\ddot{z}_{m2}$, X_4 and z_{m2} in Figs. 25 **c**, **d**, **e** and **f**. Dotted line represents X_3 and z_s in Figs. 25 **e** and **f**. Adopted from [19]

A comparison between numerical and experimental results is shown in Fig. 25. The theoretical time histories for the base acceleration $X_b^{''}$ is shown in Fig. 25(a); the accelerations of mass 1 $X_1^{''}$ (thick solid line) and mass 2 $X_4^{''}$ (thin solid line) are depicted in Fig. 25(c). The displacements of mass 1 X_1 (thick solid line), mass 2 X_4 (thin solid line) and of the specimen X_3 (dotted line) were plotted on the same graph as shown in Fig. 25(e). The numerical integrations were performed with zero initial conditions using the following values of the system parameters: $\eta_{Ls} = 2.5$, $\xi_{Ls} = 0.00255$, $\xi_s = 0.002$, $\xi_{p1} = 0.4$, $\xi_{p2} = 0.4$, $\lambda_1 = 4.36$, $\lambda_2 = 4.36$, $\vartheta = 7.828$, $\varepsilon = 0.002012$, $f_1 = 5.44$, $f_2 = 3.52$. The experimental time histories acquired are depicted in Figs. 25(b), (d) and (f). The excitation frequency and amplitude used for this experiment were 19.15Hz and 2.8mm, respectively. In these figures, Fig. 25(b) is the base acceleration $\ddot{x_b}$, Fig. 25(d) depicts the relative accelerations $\ddot{z}_{m1}$ (thick solid line) and $\ddot{z}_{m2}$ (thin solid line), and Fig. 25(f) shows the relative displacements z_{m1} (thick solid line), z_{m2} (thin solid line) and z_s (dotted line). The relative displacements of m_1 and m_2 were obtained by a double numerical integration of the relative accelerations, $\ddot{z}_{m1}$ and $\ddot{z}_{m2}$, respectively of Fig. 25(d). It can be concluded from Fig. 25 that a good qualitative and quantitative agreement between the theoretical and the experimental results was obtained.

3.4 Reduction of Two Mass Model to a Single Degree-of-Freedom System [18, 19]

The pre-loading forces from the pneumatic cylinders can be set to keep both masses and the specimen always in contact. In this case the two masses system shown in Fig. 23 can be described by Eq. (38). Consequently the model can be reduced to a single degree-of-freedom by introducing the following variables,

$$y_1 = \frac{X_1 + X_4}{2},\ \ y_2 = \frac{X_2 + X_5}{2},\ \ y_3 = X_3,\ \ z_1 = \frac{X_1 - X_4}{2},\ \ z_2 = \frac{X_2 - X_5}{2},$$

and assuming that

$$\lambda_1 = \lambda_2 = \lambda,\ \ \xi_{p1} = \xi_{p2} = \xi_p.$$

Using the new variables Eq. (38) can be re-written as follows

$$\begin{aligned}
y_1^{'} &= y_2,\\
y_2^{'} &= -\left(1 + \lambda^2 + \frac{1}{\varepsilon}\right) y_1 - (2\xi_{Ls} + 2\xi_p\lambda) y_2 + \frac{1}{\varepsilon} y_3 + \eta_{Ls}^2 \sin(\eta_{Ls}\tau),\\
y_3^{'} &= \frac{1}{\varepsilon\vartheta\xi_s} y_1 - \left(\frac{1}{\varepsilon\vartheta\xi_s} + \frac{\vartheta}{2\xi_s}\right) y_3,\\
z_1^{'} &= z_2\\
z_2^{'} &= -\left(1 + \lambda^2 + \frac{1}{\varepsilon}\right) z_1 - (2\xi_{Ls} + 2\xi_p\lambda) z_2.
\end{aligned} \tag{44}$$

As can be seen from Eq. (44), the first three equations do not depend on variable z, while the last two are independent of variable y. Hence, two independent systems have been obtained and they can be solved separately. Assuming that $X_1 = X_4$ and $X_2 = X_5$, we have $z_1 = z_2 \equiv 0$, which means that the displacements and the velocities of both masses are equal. Furthermore, for the present system, $k_{sc} \gg k_{Ls}$ and thus when $\varepsilon \to 0$, it has been assumed that the relative displacements and velocities of the springs k_{sc1} and k_{sc2} are negligible. For this case, the displacements of both masses and the specimen will be equal. Therefore, the two mass model given in Fig. 23 can be simplified to a single degree-of-freedom model as shown in Fig. 26.

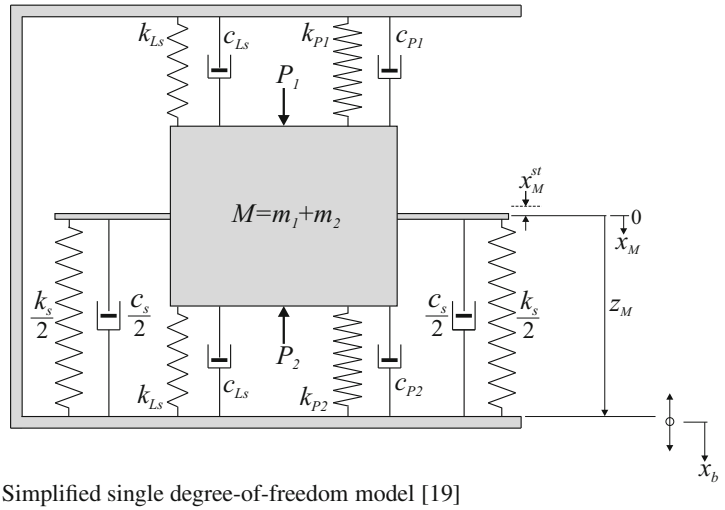

Fig. 26 Simplified single degree-of-freedom model [19]

Consequently, the dynamics of both masses can be described by the following equation of motion

$$M\ddot{z}_M + c_M\dot{z}_M + (k_M + k_s)z_M = MA_b\Omega^2\sin(\Omega t), \tag{45}$$

where,

$$z_M = \frac{z_{m1} + z_{m2}}{2} = z_{m1} = z_{m2}, \;\; M = m_1 + m_2,$$
$$c_M = (2c_{Ls} + c_{p1} + c_{p2} + c_s), \;\; k_M = (2k_{Ls} + k_{p1} + k_{p2}).$$

Transforming Eq. (45) into the non-dimensional first order differential equations, we have

$$\begin{aligned} y_1' &= y_2, \\ y_2' &= -(1+\kappa_M)y_1 - 2\xi_M y_2 + \eta_M^2\sin(\eta_M\tau), \end{aligned} \tag{46}$$

whereby the non-dimensional parameters are defined as,

$$\tau = \omega_M t, \quad \omega_M = \sqrt{\frac{k_M}{M}}, \quad \xi_M = \frac{c_M}{2M\omega_M}, \quad \kappa_M = \frac{k_s}{k_M}, \quad \eta_M = \frac{\Omega}{\omega_M},$$

where $'$ denotes $d/d\tau$.
As was demonstrated above, when both masses are in contact with the specimen, the set of equations that represent the model in Fig. 23 can be simplified from five first order equations (Eq. (44)) to just two (Eq. (46)).

3.5 Stiffness of a Cracked Beam [19]

Many investigations have been conducted to study the nonlinear effects due to discontinuous stiffness characteristics. For example externally forced piecewise linear oscillators were studied theoretically by Shaw and Holmes [51], and experimentally by Wiercigroch *et al.* [62] and Sin and Wiercigroch [53]. Obtained results in [51, 62, 53] revealed complex dynamics including existence of periodic, subharmonic and chaotic motion. The bilinear or piecewise oscillators have also been used to model the dynamic behaviour of cracked structures [66, 27, 2, 28, 9, 10, 20, 52, 6, 1]. However, the work carried out in [66, 27, 2, 28, 9, 10, 20, 52, 6, 1] assumed a stationary fatigue crack, in which, the restoring force of the cracked structure has a stiffness characteristic as shown in Fig. 27(a). In the present work, taking into account a growing fatigue crack, the stiffness of the bending specimen decreases as a function of crack length and time when crack opens. For a completely closed crack, the stiffness of a crack-free specimen is assumed. The bilinear piecewise smooth restoring force of this behaviour is shown in Fig. 27(b) for different lengthes of the crack. The main rationale behind the assumption is that, unless the remaining material at the front of the crack tip starts to yield, the decrease of the bending specimen stiffness is small even though a significant fatigue crack has propagated. Furthermore, Gudmundson [24] experimentally showed that the effect of the closing crack has a small influence on the natural frequencies, and therefore, making the assumption justified.

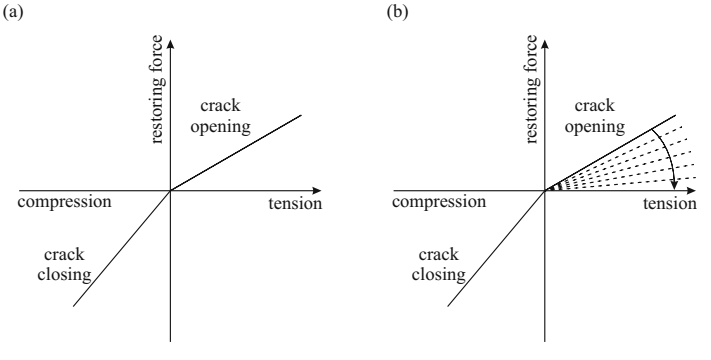

Fig. 27 Stiffness characteristics of the specimen [19]

The stiffness of the specimen with a closed crack assumed as a simply supported beam can be calculated from the formula

$$k_s^{cl} = \frac{48EI}{L_{span}^3}. \tag{47}$$

When a crack opens, the stiffness k_s^{op} can be computed from Eq. (33), which after a simple rearrangement can take the following form

$$k_s^{op} = \frac{1}{\dfrac{L_{span}^3}{48EI} + \dfrac{c_1(\alpha)+\beta c_2(\alpha)+\beta^2 c_3(\alpha)}{EB}}, \tag{48}$$

where all parameters are as defined for Eq. (33). k_s^{op} decreases in term of crack length, a, which is modelled by an exponential function of time t, [18]

$$a = a_o + a_1 \exp\left(\frac{t-a_2}{a_3}\right), \tag{49}$$

where the constants a_o, a_1, a_2 and a_3 are obtained from experiments. Eq. (49) is used to calculate the crack-depth ratio $\alpha = a/W$ in the functions $c_1(\alpha)$, $c_2(\alpha)$ and $c_3(\alpha)$ of Eq. (48).

During our fatigue tests, the two oscillating masses of the fatigue rig were kept in contact with the specimen at all time. A model that represents the full contact case was already presented in Fig. 26 and its equation of motion is given by Eq. (45). Referring to Fig. 26, for crack opening, the kinematic condition, $(z_M + x_M^{st}) > 0$, must be satisfied, and for crack closing, $(z_M + x_M^{st}) \leq 0$. After including the static forces into Eq. (45), the resulting equation was transformed to a set of two non-dimensional first order differential equations,

$$\begin{aligned} y_1^{'} &= y_2, \\ y_2^{'} &= -(1+\kappa_M)y_1 - 2\xi_M y_2 - (\rho+\kappa_M)\gamma_M + f_M + \eta_M^2 \sin(\eta_M \tau), \end{aligned} \tag{50}$$

where

$$\rho = \frac{2k_{Ls}}{k_M}, \quad f_M = \frac{P_1 + Mg - P_2}{MA_b\omega_M^2},$$

and $\gamma_M = x_M^{st}/A_b$. A Heaviside function $H(y_1+\gamma_M)$, which is equal to 1 for crack opening and 0 for crack closing is used to model the piecewise linear stiffness characteristics κ_M in Eq. (50), in which

$$\kappa_M = H(y_1+\gamma_M)\kappa_M^{op} + (1 - H(y_1+\gamma_M))\kappa_M^{cl}, \tag{51}$$

where

$$\kappa_M^{op} = \frac{k_s^{op}}{k_M}, \quad \kappa_M^{cl} = \frac{k_s^{cl}}{k_M}.$$

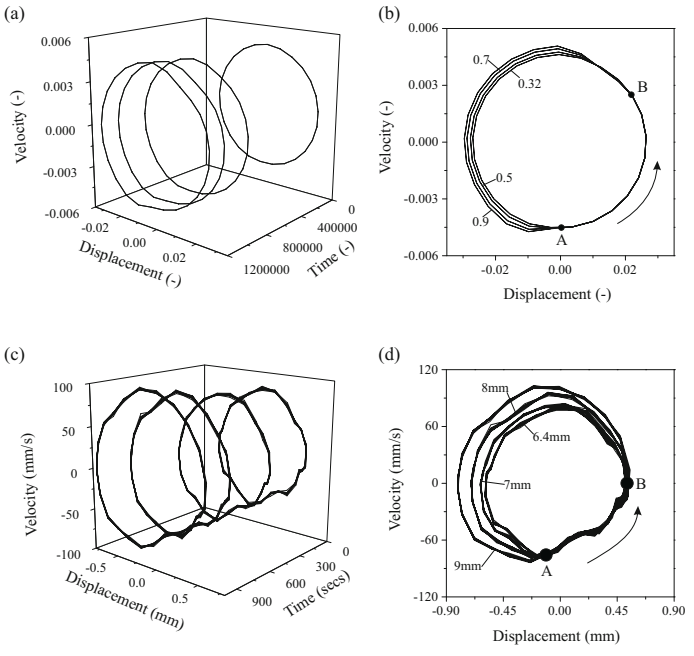

Fig. 28 Phase portraits obtained for 0N mean load and load amplitude of 274N [19]; **a** theoretical 3-dimensional, **b** theoretical 2-dimensional, **c** experimental 3-dimensional and **d** experimental 2-dimensional

A three dimensional and a two dimensional phase portraits generated from Eq. (50) representing the dynamic responses of a specimen under a growing breathing crack (crack opens and closes) are depicted in Figs. 28(a) and (b), respectively. The smallest to the largest orbits correspond to the growing crack ratio, α of 0.32, 0.5, 0.7 and 0.9, respectively. All orbits form close loops indicating period one motion with clearly visible piecewise linear nature of the dynamic responses (see Fig. 28(b)). This is due to the fact that when fatigue crack propagates, the stiffness of the specimen decreases when the crack opens, and hence, causes a larger amplitude of oscillations. In addition, the trajectories at different crack length follows the same path as the crack closes (point A to B in Fig. 28(b)), which confirms that the stiffness during the crack closure remains constant. These theoretical results were validated by the experimental phase portraits as shown in Figs. 28(c) and d.

3.6 Strange Attractor [18]

The behaviour of the system was simulated using the one mass model and the results are shown in Figs. 29 and 30. Fig. 29 presents a crack growth curve obtained for

$\xi_M = 0.014$, $\eta_M = 1.1475$, $k_s^{cl} = 14.327$, $k_s^{op} = 4.245 \times 10^{-3}(20-a)^3$ [18]. As can be seen from Fig. 29 it takes a significant time for a crack to be initiated and to start propagating. To monitor the behaviour of the system, Poincaré maps for the system with the specified crack length were constructed and they are superimposed on the crack growth curve in Fig.29. As can be seen from this figure, while the crack length remains around 5.0 mm, the system response is stable period one motion. As the crack growths, the system response is changing and at a significantly larger crack length it becomes chaotic (for example, shown strange attractors have been identified at crack length of 12.09 and 13.03 mm). As the crack increases further, a period four response was obtained at a crack length of 13.4 mm.

To observe the behaviour of the system due to the growing fatigue crack transient Poincaré maps shown in Fig. 30 were also constructed. In contrast to the standard Poincaré maps, these pictures do not reflect the steady response of the system, but give a number of snap-shots showing different dynamic responses under a growing crack. As can be seen from Fig. 30(a) when the crack length is smaller than 10.7 mm ($\tau < 900,514$), the response of the system remains period one and the location of the attractor is changing with time and the growing crack in the direction shown by the arrow. This periodic regime eventually changes into a chaotic regime for a rather short time and then, when the crack length is about 12.0 mm, the system responds with period two motion for some time as shown in Fig.30(b). Again the arrows on the plot show how the location of the attractor is changing with the growing time. Later for $\tau \approx 915,662$ we can distinguish period three motion (Fig.30(c)), for $\tau \approx 928,100$ a period two motion (Fig.30(d)) and for $\tau \approx 936,903$ a period two motion again (Fig.30(e)). All these regimes are separated by a chaotic behaviour of the system and possibly other periodic regimes which the system experiences for rather short periods of time. Thus the system with constant crack length allows us to obtain the same responses (one for each particular crack length) as was observed for the system with a growing crack.

3.7 Conclusions

In this section we presented a study on the nonlinear dynamics caused by a fatigue crack growth in a beam specimen. Specifically we investigated the behaviour of the system with a cracked specimen under periodic and chaotic loading, where the stiffness of the specimen during crack opening and closing was modelled as piecewise nonlinear function. The dynamic interactions in this system can be strongly nonlinear resulting in aperiodic responses which have an influence on the fatigue crack growth.

As conventional fatigue testing machine cannot easily generate a flexible aperiodic loading, we designed a new fatigue testing device, which was tested and modelled. The conducted experimental study revealed that chaotic excitation is more damaging for the system than the harmonic one as for the same amount of energy pumped into a specimen, the fatigue life of the specimen subjected to the aperiodic loading was significantly reduced. We developed two mathematical models of

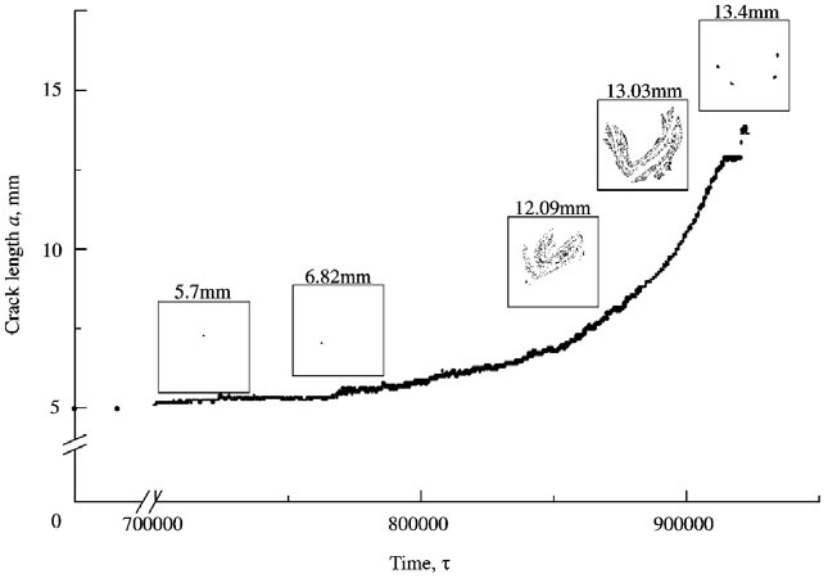

Fig. 29 Crack growth curve with superimposed Poincaré maps calculated for the system with the specified crack length obtained for $\xi_M = 0.014$, $\eta_M = 1.1475$, $k_s^{cl} = 14.327$, $k_s^{op} = 4.245 \times 10^{-3}(20 - a)^3$. Adopted from [18]

the testing device to forecast a fatigue crack growth in beam samples. Specifically the experimental rig was modelled mathematically as a two mass and one mass systems. Studying one mass system, we found that when the crack size reaches a critical value, a strange attractor is born and this phenomenon can be used in structural health monitoring. The numerical results compared with the experiments show a good correspondence.

4 Regular and Chaotic Dynamics of a Rotor System with a Bearing Clearance [33, 32, 30, 31, 45, 34]

In rotor systems a non-smoothness may appear due to bearing clearances. Physically speaking this results in piecewise nonlinear stiffness characteristics, which can consequently lead to complex nonlinear behaviour including chaotic motion. The appearance of such phenomena implies a possibility of an intermittent contact between the components of the rotor system, which is difficult to predict. Rotor systems with bearing clearances have been studied in the past, and some investigations concentrated primarily on the Jeffcott rotors. For example, Choy and Padovan [5], Muszynska and Goldman [40], Childs [4] and Chu and Zhang [7, 8] examined rubbing in rotating machinery. Ehrich [11] investigated spontaneous sidebanding,

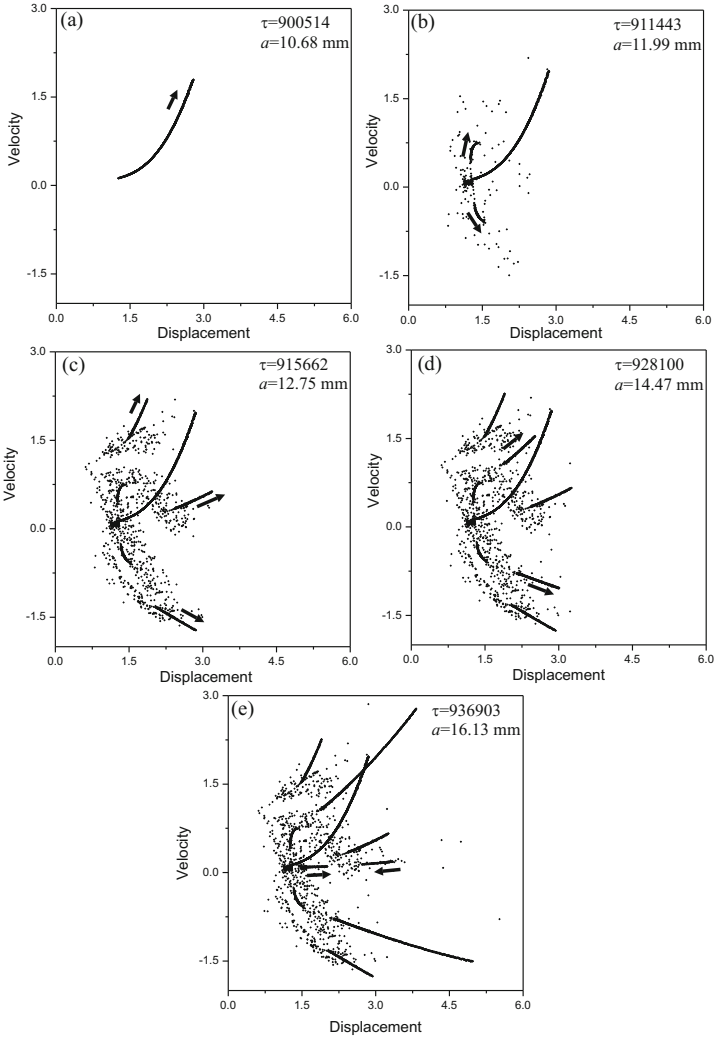

Fig. 30 Transient Poincaré maps [18] calculated for $\xi_M = 0.014$, $\eta_M = 1.1475$, $k_s^{cl} = 14.327$, $k_s^{op} = 4.245 \times 10^{-3}(20 - a)^3$, $a = 5 + 10^{-3}\exp(\tau/54734 - 7.8)$. The arrows indicate the direction of appearance of new points with the growing time

while Ganesan [21] looked at the stability analysis. Numerical investigations of the model of the Jeffcott rotor with a snubber ring presented in [33] shown the existence of multiple attractors and fractal basins of attraction. Influence of the preloading and viscous damping of the snubber ring was investigated in [31, 45], where it was shown how the preloading of the snubber ring could stabilize the dynamic responses. In this section we will discuss the work undertaken in the Centre for Applied Dynamics Research (CADR) at the University of Aberdeen. Specifically we will focuss on the finding published in [33, 32, 30, 31, 45, 34].

4.1 Physical Model and Equations of Motion [45]

The most up to date two-degrees-of-freedom model of the rotor system with a preloaded snubber ring developed by the CADR is shown in Fig. 31(a). During operation the rotor of mass M makes intermittent contact with the preloaded snubber ring and the excitation is provided by an out-of-balance rotating mass $m\rho$. It is assumed that contact is non-impulsive and that the friction between the snubber ring and the rotor is neglected. Since the mass ratio between the snubber ring and the mass of the rotor is small (for existing experimental rig it is equal to $\approx 1/17$) and the ratio between the stiffnesses of the snubber ring and the rotor is large, it is assumed that the snubber ring itself is massless. The stiffness and the viscous damping of the snubber ring are equal to k_s and c_s. The stiffness and the damping of the rotor are respectively k_r and c_r. The springs supporting the snubber ring are preloaded by Δ_x in horizontal and Δ_y in vertical directions respectively. There is a gap γ between the rotor and the snubber ring. Also in the initial position, the centre of the rotor is displaced from the centre of the snubber ring which is characterized by the eccentricity vector ε.

The presented model can operate in one of two following regimes: (a) no contact and (b) contact between the rotor and the snubber ring. In the latter regime, a preloading makes the dynamics of the system more complicated as the force acting from the snubber ring on the rotor depends on whether the displacement of the snubber ring exceeds the preloadings (in one or both directions) or not. Thus the following unique regimes can be distinguished as given in [45]:

I. No contact between the rotor and the snubber ring.
II. Contact between the rotor and the snubber ring, where the both displacements of the snubber ring are smaller than the preloadings, i.e. $|x_s| \leqslant \Delta_x$ and $|y_s| \leqslant \Delta_y$.
III. Contact between the rotor and the snubber ring, where the displacement of the snubber ring in the horizontal direction is larger than the preloading, $|x_s| > \Delta_x$, and in the vertical direction is smaller than preloading, $|y_s| \leqslant \Delta_y$.
IV. Contact between the rotor and the snubber ring, where the displacement of the snubber ring in the horizontal direction is smaller than the preloading, $|x_s| \leqslant \Delta_x$, and in the vertical direction is larger than preloading, $|y_s| > \Delta_y$.
V. Contact between the rotor and the snubber ring, where the displacements of the snubber ring are larger than the preloadings, i.e. $|x_s| > \Delta_x$ and $|y_s| > \Delta_y$.

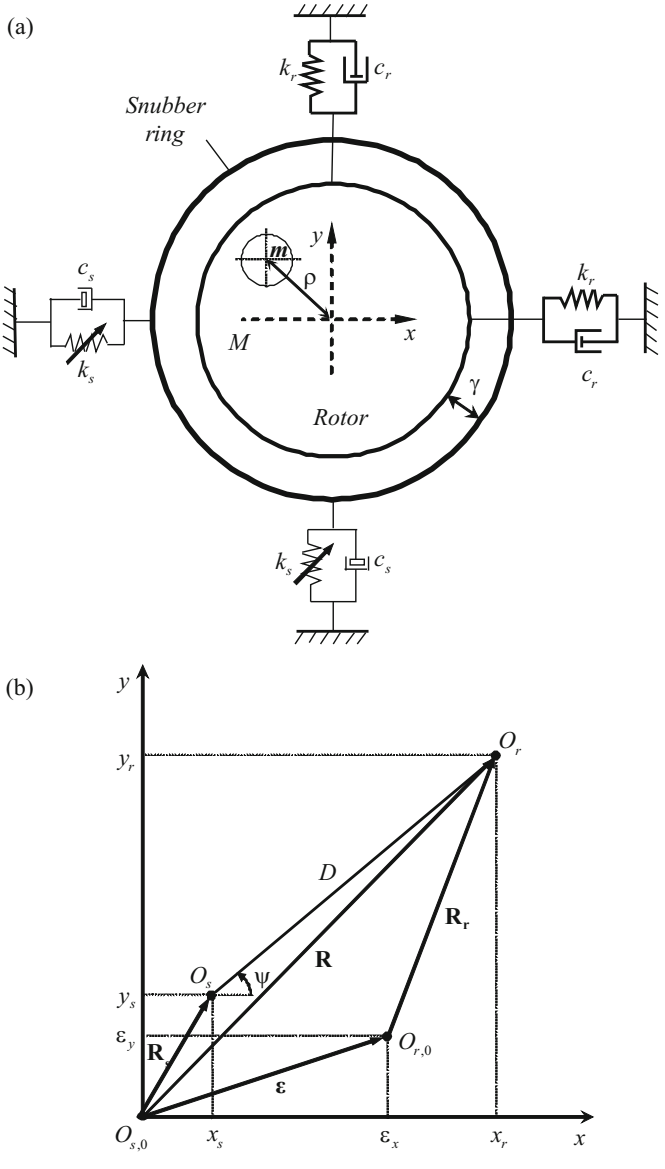

Fig. 31 **a** Physical model of the Jeffcott rotor with bearing clearance and **b** adopted coordinate system [45]

These four contact regimes were nesessary to be introduced as the results of our earlier theoretical work [32, 31] not correlating well with the experiments [30].

The co-ordinate system adopted in this section is presented in Fig. 31(b). The initial position of the rotor $O_{r,0}$ differs from the initial position of the snubber ring $O_{s,0}$ by the eccentricity vector $\varepsilon = (\varepsilon_x, \varepsilon_y)$. The vectors $\mathbf{R}_r = (x_r, y_r)$ and $\mathbf{R}_s = (x_s, y_s)$ show the current positions of the rotor and the snubber ring, and $D = \sqrt{(x_r - x_s)^2 + (y_r - y_s)^2}$ is the distance between the centres of the rotor and the snubber ring at any given time. $R = \sqrt{x_r^2 + y_r^2}$ is the radial displacement of the rotor.

For No contact regime the distance between the centres of the rotor and the snubber ring is smaller than the gap, γ, that is $R \leqslant \gamma$, and the equations of motion for the rotor and the snubber ring are

$$\begin{aligned} &M\ddot{x}_r + c_r\dot{x}_r + k_r(x_r - \varepsilon_x) = m\rho\ \Omega^2 \cos(\varphi_0 + \Omega t), \\ &M\ddot{y}_r + c_r\dot{y}_r + k_r(y_r - \varepsilon_y) = m\rho\ \Omega^2 \sin(\varphi_0 + \Omega t), \\ &k_s x_s + c_s\dot{x}_s = 0, \quad k_s y_s + c_s\dot{y}_s = 0, \end{aligned} \tag{52}$$

where φ_0 is an initial phase shift and Ω is the shaft rotational velocity.

When $D = \gamma$, the rotor contacts the snubber ring and one of the specified contact regimes occurs, for which the equations of motion can be written as

$$\begin{aligned} &M\ddot{x}_r + c_r\dot{x}_r + k_r(x_r - \varepsilon_x) + F_{s_x} = m\rho\ \Omega^2 \cos(\varphi_0 + \Omega t), \\ &M\ddot{y}_r + c_r\dot{y}_r + k_r(y_r - \varepsilon_y) + F_{s_y} = m\rho\ \Omega^2 \sin(\varphi_0 + \Omega t), \\ &x_s = x_s(x_r, y_r), \quad y_s = y_s(x_r, y_r). \end{aligned} \tag{53}$$

Here the restraining force in the snubber ring $\mathbf{F}_s = \left(F_{s_x}, F_{s_y}\right)$, shown in Fig. 32, varies for different contact regimes. The unknowns $x_s(x_r, y_r)$ and $y_s = y_s(x_r, y_r)$ give the current location of the snubber ring as a function of the current location of the rotor. To determine these functions, the principle of minimum elastic energy of the snubber ring is used.

It is worth noting that during any contact regime the distance between the centres of the rotor and the snubber ring remains constant, $D = \gamma$, despite of the fact that the force in the snubber ring, $\mathbf{F}_s$ may vary. In order to determine the moment when the contact is lost the force $\mathbf{F}_s$ should be monitored. If the projection of this force $\mathbf{F}_s$ on the vector $\mathbf{n}$ is positive (see Fig. 32), it is assumed that the rotor and the snubber ring are still in contact. Thus the contact is lost when

$$\mathbf{n} \cdot \mathbf{F}_s \leqslant 0 \quad \text{or} \quad \cos(\varphi - \psi) \leqslant 0, \tag{54}$$

where

$$\psi = \arccos\left(\frac{x_r - x_s}{\sqrt{(x_r - x_s)^2 + (y_r - y_s)^2}}\right), \qquad \varphi = \arctan\left(F_{s_y}/F_{s_x}\right).$$

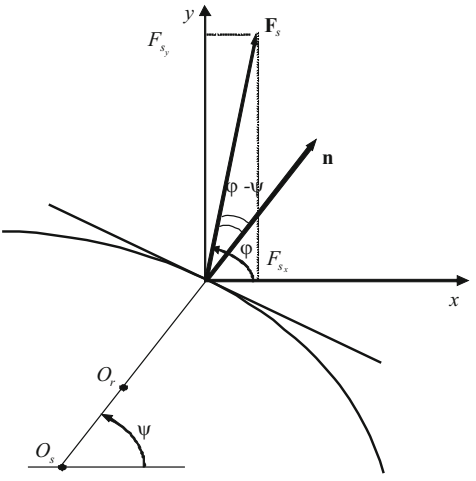

Fig. 32 Position of the force in the snubber ring $\mathbf{F}_s$ relative to the normal vector to the surface of contact [45]

Let us assume that the rotor and the snubber ring are in contact and the rotor moves the snubber ring in the direction as indicated by an arrow in Fig. 33. The forces $\mathbf{F}_1$, $\mathbf{F}_2$, $\mathbf{F}_3$ and $\mathbf{F}_4$ generated in the snubber ring as a result of the rotor and the snubber ring contact can be described in vector form as

$$\mathbf{F}_1 = \begin{cases} -\mathbf{j}\left[k_s\left(\Delta_y + y_s\right) + c_s\dot{y}_s\right], & y_s > -\Delta_y \\ 0 & y_s \le -\Delta_y \end{cases} \tag{55}$$

$$\mathbf{F}_2 = \begin{cases} \mathbf{j}\left[k_s\left(\Delta_y - y_s\right) - c_s\dot{y}_s\right], & y_s < \Delta_y \\ 0 & y_s \ge \Delta_y \end{cases} \tag{56}$$

$$\mathbf{F}_3 = \begin{cases} -\mathbf{i}\left[k_s\left(\Delta_x + x_s\right) + c_s\dot{x}_s\right], & x_s > -\Delta_x \\ 0 & x_s \le -\Delta_x \end{cases} \tag{57}$$

$$\mathbf{F}_4 = \begin{cases} \mathbf{i}\left[k_s\left(\Delta_x - x_s\right) - c_s\dot{x}_s\right], & x_s < \Delta_x \\ 0 & x_s \ge \Delta_x \end{cases} \tag{58}$$

Now the force in the snubber ring $\mathbf{F}_s$ can be conveniently defined as the resultant force taken with the opposite sign

$$\mathbf{F}_s = -\left(\mathbf{F}_1 + \mathbf{F}_2 + \mathbf{F}_3 + \mathbf{F}_4\right) \tag{59}$$

The formulae of this force for different regimes of operation are given in Table 4. These expressions for $\mathbf{F}_s$ should be substituted to Eq.(53) to obtain equations of motion for different contact regimes and to Eq. (54) to determine the moments when the contact is made or lost.

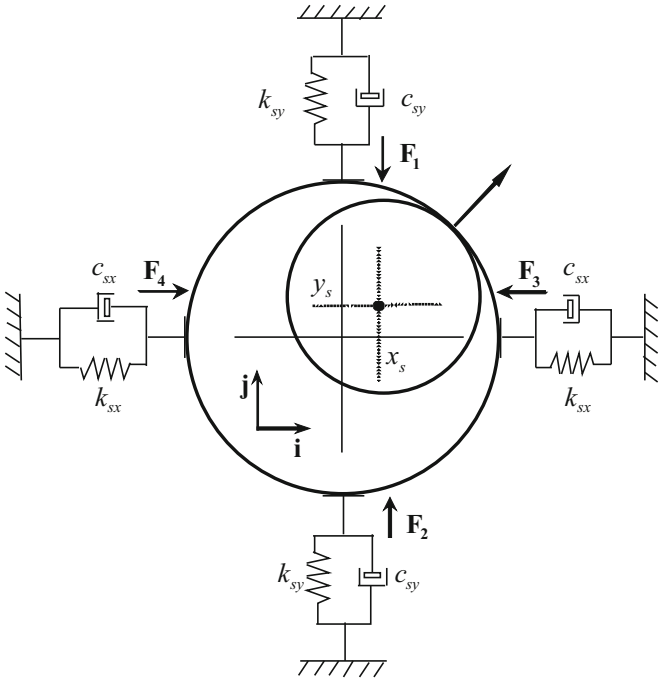

Fig. 33 Forces generated in the snubber ring [45]

Table 4 The force in the snubber ring $\mathbf{F}_s$ for various regimes

$\lvert x_s\rvert < \Delta_x$ $\lvert y_s\rvert < \Delta_y$	$\mathbf{i}\left[2k_s x_s + 2c_s\dot{x}_s\right] + \mathbf{j}\left[2k_s y_s + 2c_s\dot{y}_s\right]$
$\lvert x_s\rvert < \Delta_x$ $\lvert y_s\rvert \geq \Delta_y$	$\mathbf{i}\left[2k_s x_s + 2c_s\dot{x}_s\right] + \mathbf{j}\left[\text{sign}\,(y_s)\,k_s\left(\Delta_y + \lvert y_s\rvert\right) + c_s\dot{y}_s\right]$
$\lvert x_s\rvert \geq \Delta_x$ $\lvert y_s\rvert < \Delta_y$	$\mathbf{i}\left[\text{sign}\,(x_s)\,k_s\left(\Delta_x + \lvert x_s\rvert\right) + c_s\dot{x}_s\right] + \mathbf{j}\left[2k_s y_s + 2c_s\dot{y}_s\right]$
$\lvert x_s\rvert \geq \Delta_x$ $\lvert y_s\rvert \geq \Delta_y$	$\mathbf{i}\left[\text{sign}\,(x_s)\,k_s\left(\Delta_x + \lvert x_s\rvert\right) + c_s\dot{x}_s\right] + \mathbf{j}\left[\text{sign}\,(y_s)\,k_s\left(\Delta_y + \lvert y_s\rvert\right) + c_s\dot{y}_s\right]$

4.2 Location of the Snubber Ring and Contact Regimes

If the rotor and the snubber ring are in contact, the distance between their centres remains constant and equal to the gap, so $(x_r - x_s)^2 + (y_r - y_s)^2 = \gamma^2$. In order to find the location of the snubber ring centre when it moves and is in contact with the rotor, the following approach was adopted. It was assumed that the snubber ring being in contact with the rotor finds its position through minimum energy principle.

The potential (elastic) energy accumulated in the snubber ring at the position (x_s, y_s) is equal to the work, which is spent to bring the snubber ring to this position:

$$E = \int_{(s)} \mathbf{F}_s \cdot d\mathbf{s} = -\int_0^{x_s} (\mathbf{F_3} + \mathbf{F_4}) \cdot \mathbf{i}\, dx_s - \int_0^{y_s} (\mathbf{F_1} + \mathbf{F_2}) \cdot \mathbf{j}\, dy_s \tag{60}$$

Assuming that the dissipation of energy is negligible in comparison with the work of elastic forces, the expressions for the energy of the snubber ring take forms listed in Table 5. Consequently, the problem of finding the location of the snubber ring can be reduced to determining the minimum of the energy E with the constraint condition $D = \gamma$. This can be done using the Lagrange multipliers method by constructing the Lagrange function $L = E + \lambda\,\delta$, where λ is Lagrange multiplier, E is the elastic energy of the snubber ring, δ is the constraint function $\delta = (x_r - x_s)^2 + (y_r - y_s)^2 - \gamma^2$. As E and δ are the continuous and differentiable functions, the current position of the snubber ring (x_s and y_s) as a function of the of the current rotor position (x_r and y_r) can be determined from the conditions of the extremum existence:

$$\frac{\partial L}{\partial x_s} = 0, \qquad \frac{\partial L}{\partial y_s} = 0, \qquad \frac{\partial L}{\partial \lambda} = \delta = 0 \tag{61}$$

where $L = E + \lambda \left((x_r - x_s)^2 + (y_r - y_s)^2 - \gamma^2 \right)$.

Then by minimising the energy E with respect to the constraint $(x_r - x_s)^2 + (y_r - y_s)^2 = \gamma^2$, the functions $x_s(x_r, y_r)$ and $y_s(x_r, y_r)$ can be obtained (see Table 6).

Table 5 The elastic energy of the snubber ring E for various regimes

$\lvert x_s\rvert < \Delta_x$ $\lvert y_s\rvert < \Delta_y$	$k_s x_s^2 + k_s y_s^2$
$\lvert x_s\rvert < \Delta_x$ $\lvert y_s\rvert \geq \Delta_y$	$0.5k_s \left((\lvert x_s\rvert + \Delta_x)^2 - 2\Delta_x^2 \right) + k_s y_s^2$
$\lvert x_s\rvert \geq \Delta_x$ $\lvert y_s\rvert < \Delta_y$	$k_s x_s^2 + 0.5k_s \left((\lvert y_s\rvert + \Delta_y)^2 - 2\Delta_y^2 \right)$
$\lvert x_s\rvert \geq \Delta_x$ $\lvert y_s\rvert \geq \Delta_y$	$0.5k_s \left((\lvert x_s\rvert + \Delta_x)^2 - 2\Delta_x^2 \right) + 0.5k_s \left((\lvert y_s\rvert + \Delta_x)^2 - 2\Delta_y^2 \right)$

As explained earlier the rotor can move either in or out of contact with the snubber ring. When in contact, the force acting between the rotor and the snubber ring depends on the strength of contact and four different regimes can occur. This can be clearly explained using (x_r, y_r) plane, where each regime is mapped into an associated region as shown in Fig. 34. The boundaries between regions I, II, III, IV and V are determined from the conditions listed at the top right quadrant in Fig. 34. The equations describing these boundaries were developed and are graphically depicted

Table 6 The functions $x_s(x_r, y_r)$ and $y_s(x_r, y_r)$ for various regimes of operation

$\lvert x_s\rvert < \Delta_x$ $\lvert y_s\rvert < \Delta_y$	$x_s = x_r\left(\sqrt{x_r^2+y_r^2}-\gamma\right)\Big/\sqrt{x_r^2+y_r^2}$	$y_s = y_r\left(\sqrt{x_r^2+y_r^2}-\gamma\right)\Big/\sqrt{x_r^2+y_r^2}$
$\lvert x_s\rvert < \Delta_x$ $\lvert y_s\rvert \geq \Delta_y$	$x_s = \text{sign}(x_r)\left[\frac{2y_s(\lvert x_r\rvert+\Delta_x)}{y_r+y_s}-\Delta_x\right]$	$(y_r-y_s)^2\left((\lvert x_r\rvert+\Delta_x)^2+(y_r+y_s)^2\right)=\gamma^2(y_r+y_s)^2$
$\lvert x_s\rvert \geq \Delta_x$ $\lvert y_s\rvert < \Delta_y$	$(x_r-x_s)^2\left(\left(\lvert y_r\rvert+\Delta_y\right)^2+(x_r+x_s)^2\right)=\gamma^2(x_r+x_s)^2$	$y_s = \text{sign}(y_r)\left[\frac{2x_s(\lvert y_r\rvert+\Delta_y)}{x_r+x_s}-\Delta_y\right]$
$\lvert x_s\rvert \geq \Delta_x$ $\lvert y_s\rvert \geq \Delta_y$	$x_s = \text{sign}(x_r)\left[\frac{(\lvert x_r\rvert+\Delta_x)(\tilde{R}-\gamma)}{\tilde{R}}-\Delta_x\right]$, $\tilde{R}=\sqrt{(\lvert x_r\rvert+\Delta_x)^2+\left(\lvert y_r\rvert+\Delta_y\right)^2}$	$y_s = \text{sign}(y_r)\left[\frac{(\lvert y_r\rvert+\Delta_y)(\tilde{R}-\gamma)}{\tilde{R}}-\Delta_y\right]$

in Fig. 35, which shows one quadrant of (x_r, y_r) plane since the problem is symmetric. A detailed explanation how all these regions were determined is given below.

Region I, or No contact region is realised inside the circle

$$x_r^2 + y_r^2 = \gamma^2 \tag{62}$$

When the rotor makes a contact with the snubber ring the contact regime II begins. The boundaries of the corresponding region on (x_r, y_r) plane can be determined as follows. The inner boundary is described by Eq. (62). The outer boundaries are described by the conditions $|x_s| = \Delta_x$ and $|y_s| = \Delta_y$. Substituting x_s and y_s as the functions of x_r and y_r given in Table 6 for $|x_s| \leq \Delta_x$ and $|y_s| \leq \Delta_y$, in the first quadrant of (x_r, y_r) plane the outer boundaries are given by

$$y_r = \frac{x_r}{x_r - \Delta_x}\sqrt{\gamma^2 - (x_r - \Delta_x)^2}, \tag{63}$$

$$x_r = \frac{y_r}{y_r - \Delta_y}\sqrt{\gamma^2 - (y_r - \Delta_y)^2}. \tag{64}$$

If the rotor pushes the snubber ring strongly enough in the horizontal direction, i.e. its displacement, x_s becomes larger than the preloading Δ_x, the regime III begins. The inner (left) border for the region III is described by Eq. (63) and outer (upper) border again is governed by the conditions $|y_s| = \Delta_y$. As this border is simultaneously the inner (lower) border for the region V, the explicit expression for y_s as function of x_r and y_r (Table 6) for $|x_s| > \Delta_x$ and $|y_s| > \Delta_y$ is used

$$x_r = -\Delta_x + \frac{y_r + \Delta_y}{y_r - \Delta_y}\sqrt{\gamma^2 - (y_r - \Delta_y)^2}. \tag{65}$$

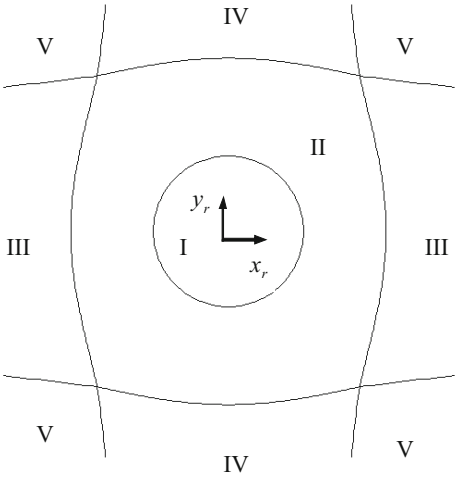

Fig. 34 Regions of operation for a rotor system with a symmetrically preloaded snubber ring in (x_r, y_r) plane [45]

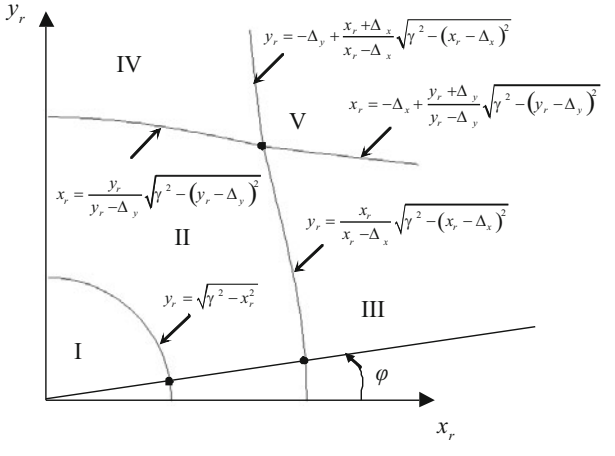

Fig. 35 Regions of operation and their boundaries for the first quadrant of (x_r, y_r) plane [45]

In the same way for the rotor moving in the region IV, one can obtain the inner (lower) border for the region IV as described by Eq. (64) and the outer (right) border as

$$y_r = -\Delta_y + \frac{x_r + \Delta_x}{x_r - \Delta_x}\sqrt{\gamma^2 - (x_r - \Delta_x)^2}. \tag{66}$$

Finally, the inner borders of the region V are described by Eq. (65) and (66).

4.3 Numerical Simulations

Numerical results presented in this section are to illustrate the use of the developed analytical formulas and to show the influence of the preloading on the dynamics of the rotor crossing different regions of operation. The calculations were performed in the dimensionless domain by defining the following dimensionless variables

$$\tau = \omega_n t, \quad \mathbf{f}_s = \frac{\mathbf{F}_s}{k_r \gamma}, \quad \hat{x}_r = \frac{x_r}{\gamma}, \quad \hat{y}_r = \frac{y_r}{\gamma}, \quad \hat{x}_s = \frac{x_s}{\gamma}, \quad \hat{y}_s = \frac{y_s}{\gamma}, \quad v_{x_s} = \hat{x}_s',$$

and parameters

$$\eta = \frac{\Omega}{\omega_n}, \quad \nu_1 = \frac{c_r}{2\sqrt{k_r M}}, \quad \nu_2 = \frac{c_s}{2\sqrt{k_r M}}, \quad \eta_m = \frac{m}{M}, \quad \hat{\rho} = \frac{\rho}{\gamma},$$
$$\hat{K} = \frac{k_s}{k_r}, \quad \hat{\varepsilon}_x = \frac{\varepsilon_x}{\gamma}, \quad \hat{\varepsilon}_y = \frac{\varepsilon_y}{\gamma}, \quad \hat{\Delta}_x = \frac{\Delta_x}{\gamma}, \quad \hat{\Delta}_y = \frac{\Delta_y}{\gamma}.$$

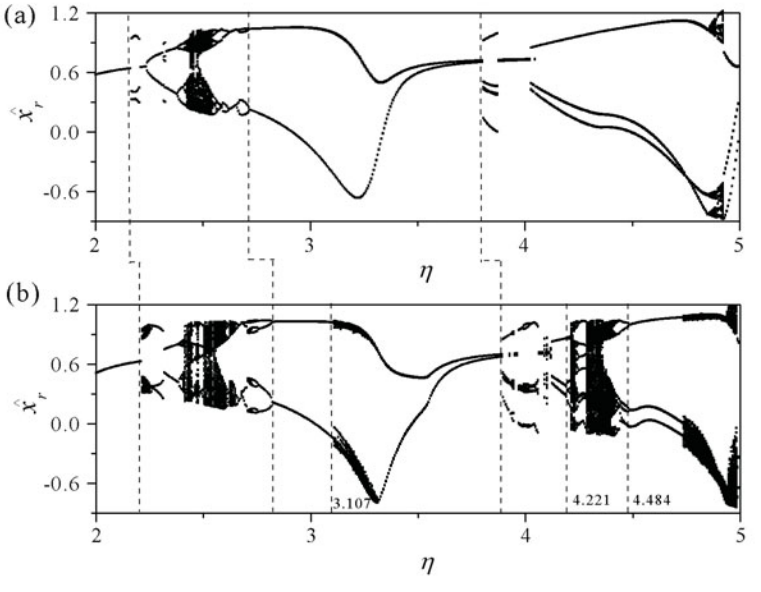

Fig. 36 Bifurcation diagrams showing the displacement of the rotor as function of frequency $\hat{x}_r(\eta)$ calculated for **a** $\hat{\Delta}_x = \hat{\Delta}_y = 0$; **b** $\hat{\Delta}_x = \hat{\Delta}_y = 0.1$; and $\nu_1 = 0.125$, $\nu_2 = 0.002$, $\hat{K} = 30$, $\eta_m = 0.0017$, $\hat{\rho} = 70$, $\hat{\varepsilon}_x = 0.9$ and $\hat{\varepsilon}_y = 0$. Adopted from [45]

In this study numerous bifurcation diagrams were constructed including the two shown in Fig. 36 for the displacement of the rotor $\hat{x}_r$ under varying the frequency ratio η for the unpreloaded (Fig. 36(a)) and the preloaded (Fig. 36(b)) cases. The

control parameter η was set to the leftmost value 2. Starting with zero initial conditions first 300 cycles were disregarded to ensure that steady state solutions had been reached. The displacement $\hat{x}_r$ for the next 150 cycles was plotted. Then a small increment was added to the control parameter and the procedure was repeated until the control parameter reached the rightmost value $\eta = 5$. The parameters used in numerical computations were as follows: $\nu_1 = 0.125$, $\nu_2 = 0.002$, $\hat{K} = 30$, $\eta_m = 0.0017$, $\hat{\rho} = 70$, $\hat{\varepsilon}_x = 0.9$ and $\hat{\varepsilon}_y = 0$. The preloading was set to zero in both directions for Fig. 36(a), and $\hat{\Delta}_x = \hat{\Delta}_y = 0.1$ for Fig. 36(b). As can be clearly seen from Fig. 36 the preloading changes the bifurcation structure. Firstly, it shifts the bifurcation points towards higher frequencies; dash lines in Fig. 36 point out such behaviour. For instance, the period one observed in the beginning of the diagram bifurcates at $\eta = 2.165$ for unpreloaded and at $\eta = 2.213$ for preloaded case. The bifurcation of period four motion into period two motion moves from $\eta = 2.717$ to 2.824, and the period two bifurcates into period four at $\eta = 3.803$ and 3.893 for unpreloaded and preloaded cases respectively. Secondly, the introduction of the preloading changes the character of bifurcations. For example, the period one motion marked by the leftmost dash line, bifurcates into period three motion (see Poincaré map in Fig. 37(a)) for the unpreloaded case and into quasi-periodic motion (Fig. 37(b)) for the preloaded case. Also the preloading changes the structure of the chaotic attractor which be seen from Poincaré maps shown in Fig. 37(c) and 37(d) calculated at $\eta = 2.442$ for the unpreloaded and the preloaded cases. Finally and most importantly the preloading introduces new bifurcations and new regimes. For example, an additional bifurcation of the period two motion into quasi-periodic motion appears at $\eta \approx 3.107$ for the preloaded case.

The changes in dynamical behaviour are even more visible in $(\hat{x}_s, \hat{v}_{x_s})$ plane. The comparisons between trajectories of the snubber ring on the phase plane $(\hat{x}_s, \hat{v}_{x_s})$ for the system with and without preloading are presented in Fig. 38. The dynamics of the snubber ring is shown in Figs. 38(a) and 38(c) for the case without preloading ($\hat{\Delta}_x = \hat{\Delta}_y = 0$), and in Figs. 38(b) and 38(d) for the case with preloading ($\hat{\Delta}_x = \hat{\Delta}_y =$ 0.05 and 0.03 respectively). As can be seen from the Fig. 38 in both cases, velocity of snubber ring $\hat{v}_{x_s}$ experiences a jump at $\hat{x}_s = 0$, when the rotor hits the snubber ring. For the systems with preloading there is an additional jump of velocity $\hat{v}_{x_s}$, which appears at $\hat{x}_s = \hat{\Delta}_x$. It can be also observed that the preloading reduces the amplitude of the snubber ring vibrations.

4.4 Experimental Verification

The results of the mathematical modelling were verified on a purpose designed experimental rig. Figure 39(a) shows the rotor rig which comprises of essentially two main parts, a rigid rotor (1), visco-elastically supported by four flexural rods (2) and excited by the out-of-balance mass (3), and a snubber ring (4) also elastically supported using four compression springs. The rotor assembly consists of a steel rotor, running in two angular contact bearings. Holes (5) were drilled and tapped in both

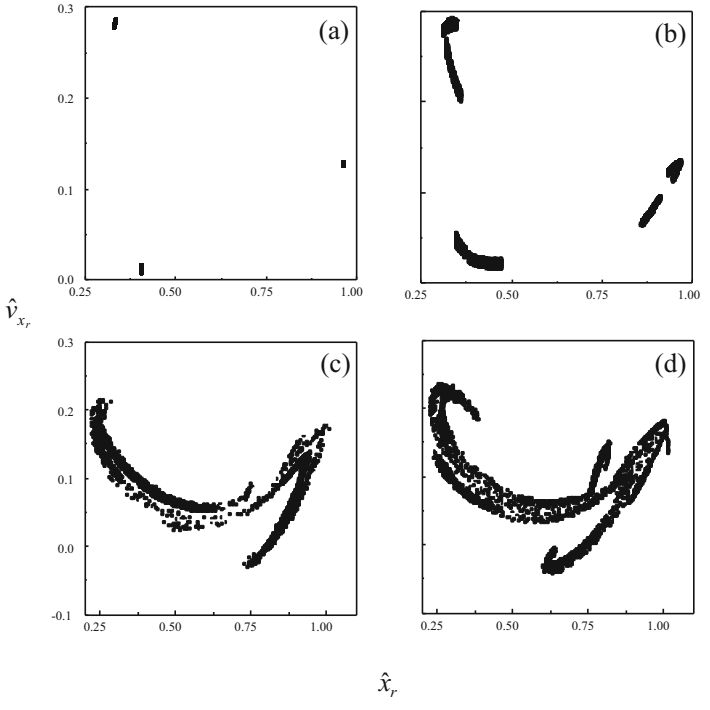

Fig. 37 Poincaré maps $\hat{v}_{x_r}(\hat{x}_r)$ [45] calculated for **a**, **c** $\hat{\Delta}_x = \hat{\Delta}_y = 0$; **b**,**d** $\hat{\Delta}_x = \hat{\Delta}_y = 0.1$; and $\nu_1 = 0.125$, $\nu_2 = 0.002$, $\hat{K} = 30$, $\eta_m = 0.0017$, $\hat{\rho} = 70$, $\hat{\varepsilon}_x = 0.9$ and $\hat{\varepsilon}_y = 0$; and **a** $\eta = 2.223$, **b** $\eta = 2.181$ and **c**, **d** $\eta = 2.442$

inner sleeves for the addition of imbalance weights. A pair of viscous dampers (6) was attached to the rotor to provide the system with heavier damping.

Four flexural rods (2) are clamped symmetrically at one end to the outer bearing housing and at the other to a large support block. The support block (7) is in turn bolted to a large cast iron bed. The stiffness of the snubber ring is provided by four compression springs (8), of much greater stiffness than that of the flexural rods. The rotor ran inside the ring, with a radial clearance between the ring (4) and the outer bearing housing (1). Two different outer rings were used in the experiments one with a 0.5 mm and another with 0.75 mm gap.

The rotor is driven by a variable speed DC motor (9). The shaft speed monitoring disc has a notch cut into it, which is aligned with the imbalance mass. As the notch passes a light-emitting-diode optoswitch, a once-per-revolution phase signal is obtained. The displacements of the rotor system are monitored by non-contacting eddy current probes. The displacement and forcing frequency signals were collected by a Labview data acquisition system with a custom written program controlling the rate of sampling, the number of samples, calibration and computation of the rotational frequency. The relative velocities of the rotor and the snubber ring $\dot{x}_r$, $\dot{y}_r$, $\dot{x}_s$ and $\dot{y}_s$

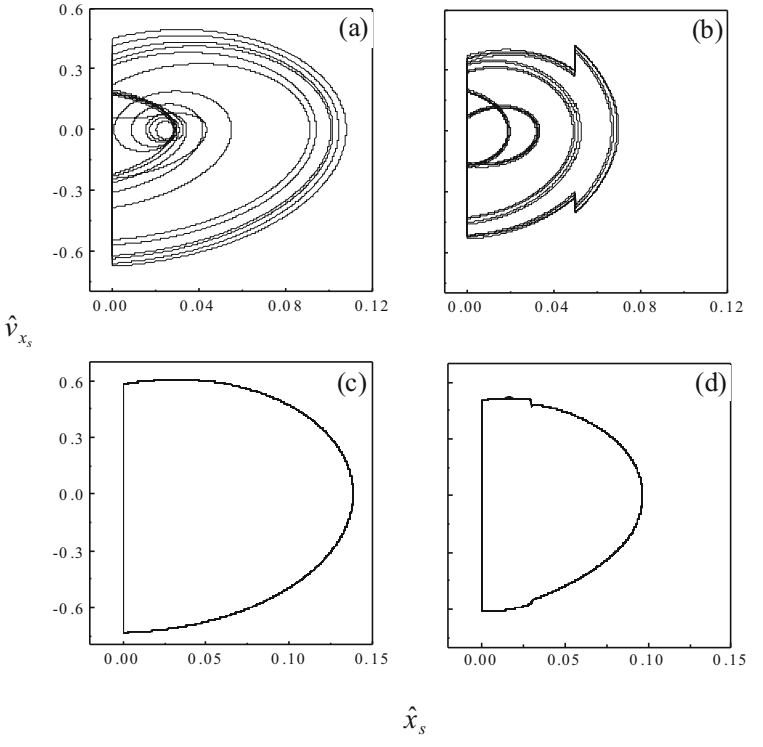

Fig. 38 Phase portraits $\hat{v}_{x_s}(\hat{x}_s)$ calculated for **a** $\hat{\Delta}_x = \hat{\Delta}_y = 0$; **b** $\hat{\Delta}_x = \hat{\Delta}_y = 0.05$; and $\nu_1 = 0.06$, $\nu_2 = 0.002$, $\eta = 2.5$, $\hat{K} = 30$, $\eta_m = 0.00289$, $\hat{\rho} = 70$, $\hat{\varepsilon}_x = 0.4$ and $\hat{\varepsilon}_y = 0.5$; and **c** $\hat{\Delta}_x = \hat{\Delta}_y = 0$; **d** $\hat{\Delta}_x = \hat{\Delta}_y = 0.03$ and $\nu_1 = 0.125$, $\nu_2 = 0.002$, $\eta = 3.0$, $\hat{K} = 30$, $\eta_m = 0.0017$, $\hat{\rho} = 70$, $\hat{\varepsilon}_x = 0.9$ and $\hat{\varepsilon}_y = 0$. Adopted from [45]

were calculated from the displacements measured by the eddy current probes. The data was collated on the computer, where it was scaled, plotted and analysed in the form of Poincaré maps and bifurcation diagrams.

Now a sample of extensive experimental studies [30] conducted to verify the mathematical model of Jeffcott rotor system with a preloaded snubber ring [45] is presented here. The following values of the system parameters were chosen: the rotor mass and mass of the out-of-balance were $M = 9.7$ kg and $m = 0.028$ kg respectively. The combined stiffness of the rods supporting the rotor was $k_{r_x} = k_{r_y} =$ 79 kN/m, which yields a natural frequency of 14.4 Hz. The snubber ring stiffness was $k_s = 2354$ kN/m and the equivalent viscous damping from the rods and the dampers in the horizontal and vertical directions was the same and equal to $c_{r_x} = c_{r_y} = 1050$ N/s. The out-of-balance radius, was $\rho = 35$ mm.

When constructing the bifurcation diagrams, the forcing frequency (the shaft rotational speed) was varied between 7 and 30 Hz and for some tests up to 50 Hz to

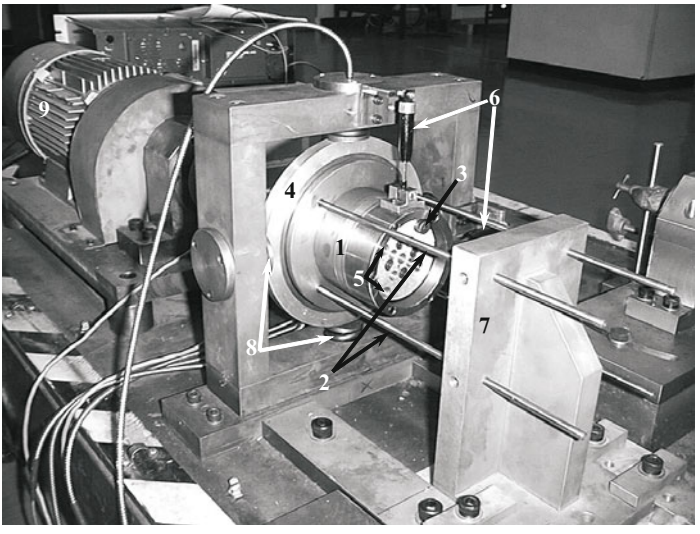

Fig. 39 Photograph of the experimental Jeffcott rotor [34]

examine the global bifurcations. The system responses were investigated by collecting data with the forcing frequency steps of around 1 Hz. The continuation method was applied, so for each frequency the initial conditions were taken from the previous examined frequency discarding about 400 cycles in order to ensure the steady-state behaviour is reached.

The bifurcation diagrams presented in Fig. 40 give a comparison of the theoretical (Fig. 40(a)) and the experimental (Fig. 40(b)) responses showing a good degree of correspondence. In both figures a wide range of chaotic regimes is observed, separated by period one, two and three regimes. Here chaotic attractors shown as Poincaré maps were obtained for two different values of the frequency: $f = 30.1$ Hz, and $f = 37.1$ Hz keeping the remaining parameters constant: $k_s = 2354$ kN/m, $k_{r_x} = k_{r_y} = 79$ kN/m, $c_{r_x} = c_{r_y} = 105$ kg/s, $c_s = 3.5$ kg/s, $M = 9.7$ kg, $m = 0.028$ kg, $\rho = 35$ mm, $\gamma = 0.5$ mm, $\varepsilon_x = 0.5$ mm, $\varepsilon_y = 0$ mm and $\Delta_x = \Delta_y = 0.1$ mm. It is apparent that the theoretical and experimental attractors are topologically similar.

In the next presented experiment the eccentricity ratios were set up as $\varepsilon_x = 0.45$ mm and $\varepsilon_y = 0.05$ mm. The bifurcation diagrams constructed theoretically and experimentally for this case are presented in Fig. 41. Because only period one motion regime exists in the interval $f \in (30, 50)$ Hz, the maximum forcing frequency for these diagrams was reduced to 30 Hz. Comparing with the previously shown diagrams of Fig. 40, here the eccentricity change leads the transition from period one motion to chaos through period doubling bifurcations. The experimental result of Fig. 41(b) follows all the basic bifurcations observed theoretically such as the period doubling bifurcation at $f \approx 14.74$ Hz and the boundary crisis at $f \approx 26.1$ Hz. Phase portraits for the periodic and chaotic cross-sections were plotted for $f = 17.6$ Hz and

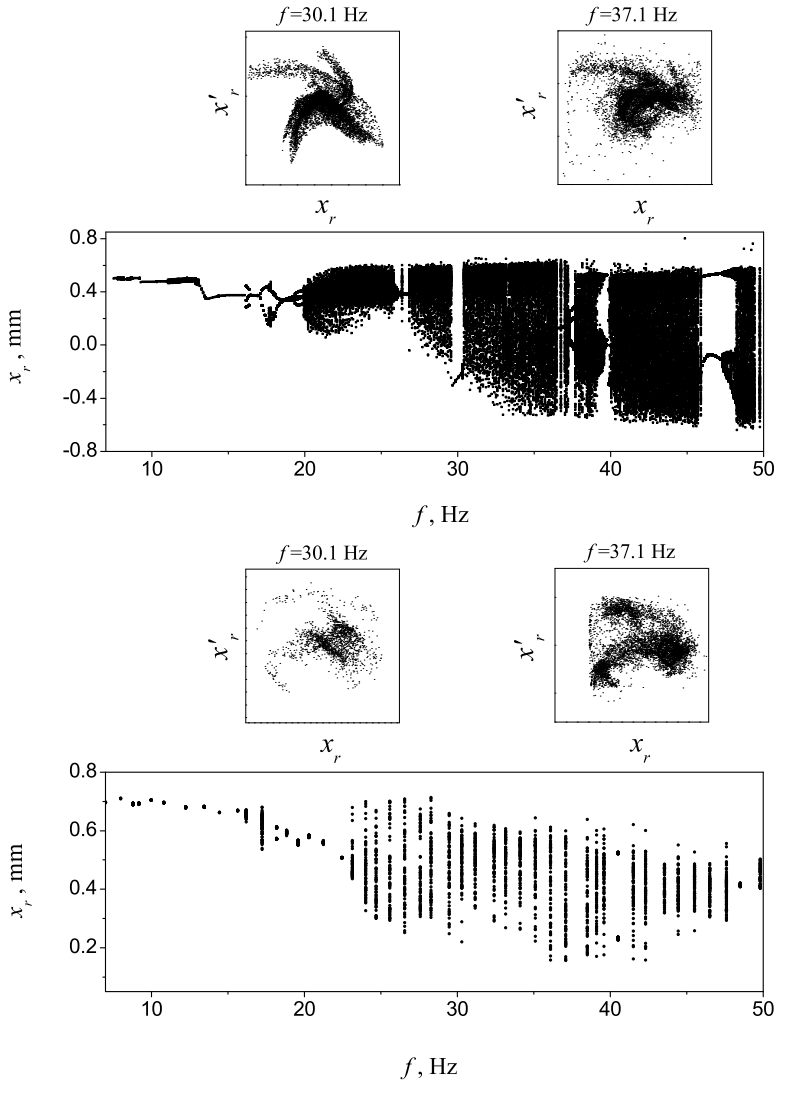

Fig. 40 Bifurcation diagrams for the forcing frequency [30] **a** theoretical and **b** experimental; $k_s = 2354$ kN/m, $k_{r_x} = k_{r_y} = 79$ kN/m, $c_{r_x} = c_{r_y} = 105$ kg/s, $c_s = 3.5$ kg/s, $M = 9.7$ kg, $m = 0.028$ kg, $\rho = 35$ mm, $\gamma = 0.5$ mm, $\varepsilon_x = 0.5$ mm, $\varepsilon_y = 0$ mm and $\Delta_x = \Delta_y = 0.1$ mm

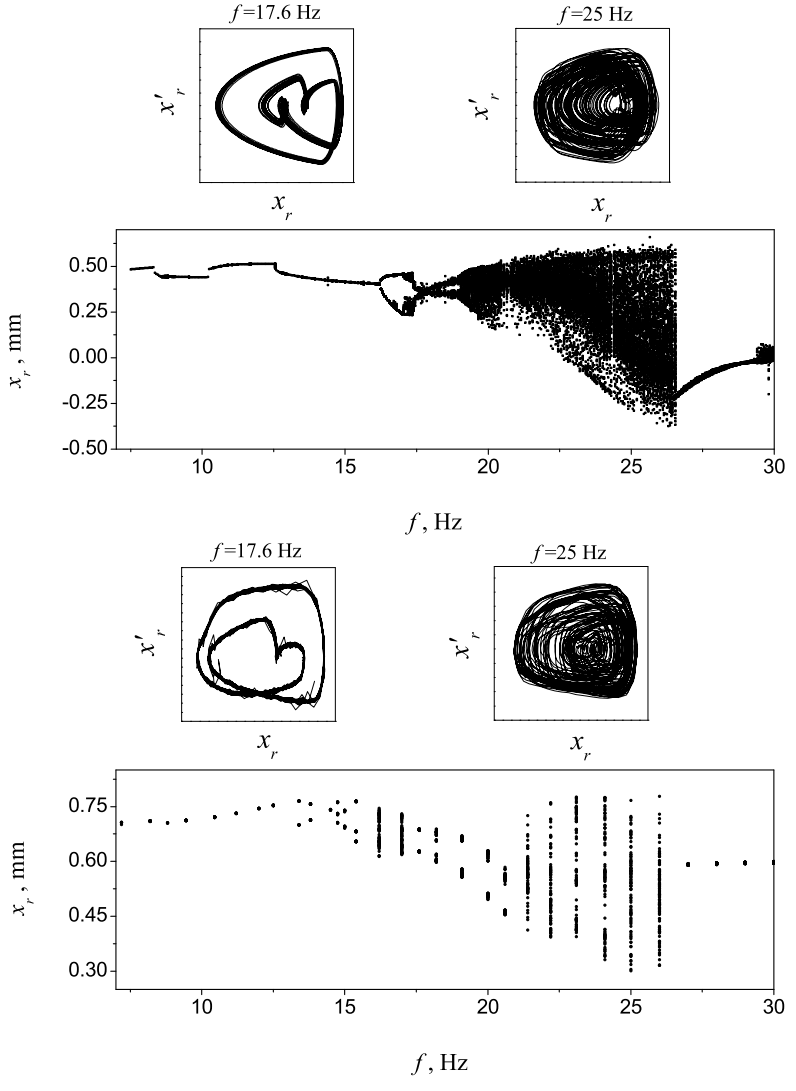

Fig. 41 **a** Theoretical and **b** experimental bifurcation diagrams [34] for the forcing frequency where $k_s = 2354$ kN/m, $k_{r_x} = k_{r_y} = 79$ kN/m, $c_{r_x} = c_{r_y} = 105$ kg/s, $c_s = 3.5$ kg/s, $M = 9.7$ kg, $m = 0.028$ kg, $\rho = 35$ mm, $\gamma = 0.5$ mm, $\varepsilon_x = 0.45$ mm, $\varepsilon_y = 0.05$ mm and $\Delta_x = \Delta_y = 0.04$ mm

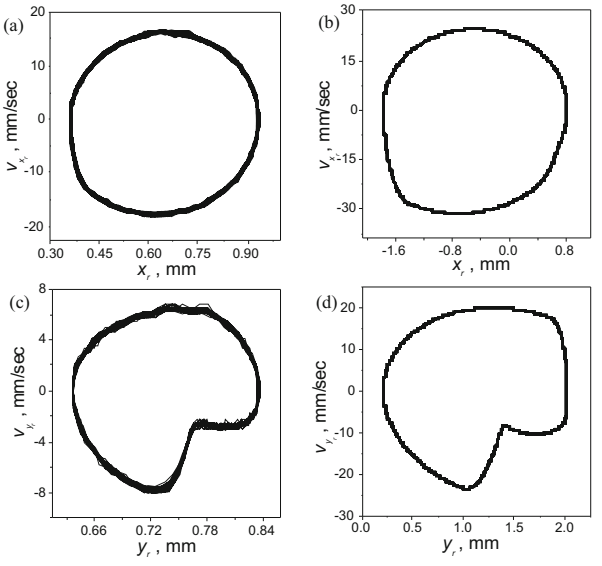

Fig. 42 **a**, **c** Experimental and **b**, **d** theoretical phase portraits for periodic behaviour of the Jeffcott rotor system in $x-$ and $y-$directions for the cross-section $f = 13.1$ Hz. Adopted from [34]

for $f = 25$ Hz showing also a good correspondence. Furthermore, the phase portraits in the x and y directions for periodic trajectories were examined at $f = 13.1$ Hz and are shown in Fig. 42. The experimental phase portraits in the $x-$ and $y-$directions are plotted in Fig. 42(a) and (c), and the corresponding to them theoretical graphs are depicted in Fig. 42(b) and (d). As can be seen, again the theoretical predictions correspond well to the experimental results.

Examining the system responses for different values of the forcing frequency shown in Figs. 40 and 41, it is clear from the bifurcation diagrams and phase planes that periodic regimes dominate at low and at high frequencies. The periodic regimes for the low frequency are caused by insufficient excitation of the rotor and as a result either there is no contact between the rotor and the snubber ring or just one contact per period. As the forcing frequency is increased, and the amplitude of oscillations rises the impacts between the rotor and the ring become stronger and the system generates chaotic vibration. The periodic regimes observed for the high frequencies have a wide range and lower amplitude of vibration than chaotic ones. In summary, the experimental results correspond well with the theoretical predictions.

4.5 Conclusions

In this section a rotor system with bearing clearance was investigated in order to gain understanding of its complex dynamic responses. First we discussed the mathematical model developed at the Centre for Applied Dynamics Research. The model

which is a Jeffcott rotor with an elastic preloaded snubber ring was formulated as a piecewise nonlinear system operating in one of five distinct regimes of operation: one of no contact and four of different types of contact. The boundaries between those regions were determined analytically and the equations of motion were formulated.

The undertaken numerical simulation shows significant differences in the system behaviour for the cases without and with preloading of the snubber ring. Specifically, the constructed bifurcation diagrams show the tendency to shift the bifurcation points towards higher frequencies for the preloaded cases. It was also found that the character of the bifurcations changes for the cases with preloading, and new bifurcations and regimes were observed in these cases. In particular, chaotic vibrations within a wider range of excitation frequency were obtained. In addition, we found that the periodic response tends to occur at the lower and higher frequencies.

The theoretical predictions were verified experimentally on the rig developed in Aberdeen. A good degree of correlation was found for the wide range of system parameters.

5 Conclusions

In this chapter we studied an important phenomenon of non-smoothness occurring in dynamical systems, and very common in engineering applications. Mathematically, such systems can be described as piecewise smooth as suggested in Fig. 1. Hence, their global solutions can be obtained by stitching local solutions, which are easy to determine by standard methods. For example, a global solution for a piecewise linear smooth dynamical system often leads to a set of nonlinear algebraic equations.

Three mechanical engineering systems were modelled and analysed in order to illustrate an approach which has been developed by the Centre for Applied Dynamics Research at Aberdeen to study non-smooth dynamical systems. Firstly, the vibro-impact moling device was investigated in order to understand how to maximise its progression rates. Applying the developed methodology, in this case periodic trajectories were reconstructed as they go through three linear subspaces (*No contact*, *Contact with progression* and *Contact without progression*), and using combination of analytical and numerical methods the optimal range of the system parameters was identified. The conducted analysis revealed that the best progression rates are achieved for low frequencies and the ratio between the dynamic and static forces around 2.

In the second considered application the influence of opening and closing of a fatigue crack on the entire system dynamics was modelled and analysed. Specifically, we were interested in the aperiodic behaviour and therefore a novel apparatus to induce aperiodic loading to a beam specimen with a fatigue crack was developed. It was shown experimentally that fatigue life can be reduced few times if the sample is loaded aperiodically. The experimental rig was modelled as two and one mass system depending whether the contact between the loadings and the sample is lost

or not. The analysis of the developed mathematical model shown that as a crack grows linearly before reaching its critical value, the response of the system remains periodic. When its size exceeds the critical value, the system behaviour becomes chaotic and then the crack growth increases exponentially. This phenomenon can be used in structural health monitoring.

Finally, we investigated a problem from rotordynamics, where nonlinear interactions between the rotor and the snubber ring were studied. We discussed the most up-to-date model and the experimental rig developed to understand the complex behaviour of this system. The rotor system can operate in one of five regimes, which were determined analytically. The influence of the preloading of the snubber ring on the system behaviour was investigated and the range of the system parameters where chaotic vibrations occur was identified. The results obtained from the developed mathematical model confronted with the experiments shown a good degree of correlation.

Acknowledgements. The financial support from EPSRC, Rolls-Royce, Scottish Enterprise and the European Commission is gratefully acknowledged. Also we would like to thank our former PhD students and collaborators including E.V. Karpenko (Aberdeen), W.F. Deans (Aberdeen), N.Jaksic (Ljubljana), M.Boltežar (Ljubljana), M.P. Cartmell (Glasgow), R.D. Neilson (Aberdeen), A.M. Krivtsov (St.Petersburg), C.Grebogi (Sao Paulo), K.C. Woo (Aberdeen), A.A. Rodger (Aberdeen), B. de Kraker (Eindhoven), V.M.T. Sin (Aberdeen), K. Li (Michigan).

References

1. Abraham, O.N.L., Brandon, J.: A piecewise linear approach for the modelling of a breathing crack. In: 17th International Seminar on Modal Analysis, Leuven, Belgium, pp. 417–431 (1992)
2. Actis, R.L., Dimarogonas, A.D.: Non-linear effects due to closing cracks in vibration beams. In: 12th ASME Conference on Mechanical Engineering, Vibration and Noise, Montreal, Canada, pp. 99–104 (1989)
3. Anderson, T.L.: Fracture mechanics - Fundamental and applications. CRC Press, Boca Raton (1994)
4. Childs, D.W.: Fractional-frequency rotor motion due to nonsymmetric clearance effects. Trans. ASME, Journal of Engineering for Power 104(3), 533–541 (1982)
5. Choy, F.K., Padovan, J.: Non-linear transient analysis of rotor-casing rub events. Journal of Sound and Vibration 113(3), 529–545 (1987)
6. Chu, Y.C., Shen, M.-M.H.: Analysis of forced bilinear oscillators and the application to cracked beam dynamics. AIAA Journal 30, 2512–2519 (1992)
7. Chu, F., Zhang, Z.: Periodic, quasi-periodic and chaotic vibrations of a rub-impact rotor system supported on oil film bearing. International Journal of Engineering Sciences 35, 963–973 (1997)
8. Chu, F., Zhang, Z.: Bifurcation and chaos in a rub-impact jeffcott rotor system. J. Sound Vibr. 210, 1–18 (1998)
9. Collins, K.R., Plaut, R.H., Wauer, J.: Detection of cracks in rotating Timoshenko shafts using axial impulses. Journal of Vibration, Acoustics, Stress, and Reliability in Design, Trans. ASME 113, 74–78 (1991)

10. Collins, K.R., Plaut, R.H., Wauer, J.: Free and forced longitudinal vibrations of a cantilvered bar with a crack. Journal of Vibration, Acoustics, Stress, and Reliability in Design, Trans. ASME 114, 171–177 (1992)
11. Ehrich, F.F.: Spontaneous sidebanding in high-speed rotordynamics. Trans. ASME, J. Vibr. Acoust. 114, 498–505 (1992)
12. Ebrahimi, S., Eberhard, P.: Rigid-elastic modeling of meshing gear wheels in multibody systems. Multibody System Dynamics 16(1), 55–71 (2006)
13. Feeny, B.: A non-smooth Coulomb friction oscillator. Physica D 59, 25–38 (1992)
14. Filippov, A.F.: Differential equations with discontinuous right-hand side. American Mathematical Society Translations 42(2), 199–231 (1978)
15. Foong, C.H.: Influence of fatigue crack growth on the dynamics of engineering components and structures, PhD thesis, University of Aberdeen (2004)
16. Foong, C.H., Wiercigroch, M., Deans, W.F.: Novel dynamic fatigue-testing device: Design and measurements. Measurement Science and Technology 17, 2218–2226 (2006)
17. Foong, C.H., Jakšić, N., Wiercigroch, M., Boltežar, M.: Parameter identification of the fatigue-testing rig. International Journal of Mechanical Sciences 50, 1142–1152 (2008)
18. Foong, C.H., Pavlovskaia, E., Wiercigroch, M., Deans, W.F.: Chaos caused by fatigue crack growth. Chaos, Solitons and Fractals 16, 651–659 (2003)
19. Foong, C.H., Wiercigroch, M., Pavlovskaia, E., Deans, W.F.: Nonlinear vibration caused by fatigue. Journal of Sound and Vibration 303, 58–77 (2007)
20. Friswell, M.I., Penny, J.E.T.: A Simple Nonlinear Model of a Cracked Beam. In: 10th International Modal Analysis Conference, San Diego, California, USA, pp. 516–521 (1992)
21. Ganesan, R.: Dynamic response and stability of a rotor-support system with non-symmetric bearing clearances. Mechanism Machine Theory 31, 781–798 (1996)
22. Gonsalves, H.D., Neilson, R.D., Barr, A.D.S.: A study of the response of a discontinuously nonlinear rotor system. Nonlinear Dynamics 7, 451–470 (1995)
23. Grabec, I.: Chaotic dynamics of the cutting process. International Journal of Machine Tools and Manufacture 28, 19–32 (1988)
24. Gudmundson, P.: The dynamic behaviour of slender structures with cross-sectional cracks. Journal of the Mechanics and Physics of Solids 31, 329–345 (1983)
25. Guinea, G.V., Pastor, J.Y., Elices, M.: Stress intensity factor, compliance and CMOD for a general three-point-bend beam. International Journal of Fracture 89, 103–116 (1998)
26. Hsu, C.S.: Cell-To-Cell Mapping: A Method of Global Analysis for Nonlinear Systems. Springer, Heidelberg (1987)
27. Ibrahim, A., Ismail, F., Martin, H.R.: Modelling of the dynamics of a continuous beam including nonlinear fatigue crack. International Journal of Analytical and Experimental Modal Analysis 2, 76–82 (1987)
28. Ismail, F., Ibrahim, A., Martin, H.R.: Identification of fatigue cracks from vibration testing. Journal of Sound and Vibration 140, 305–317 (1990)
29. Kahraman, A., Singh, R.: Non-linear dynamics of a spur gear pair. Journal of Sound and Vibration 142(1), 49–75 (1990)
30. Karpenko, E.V.: Nonlinear dynamics of a Jeffcott rotor with imperfections, PhD Thesis, University of Aberdeen (2003)
31. Karpenko, E.V., Pavlovskaia, E.E., Wiercigroch, M.: Bifurcation analysis of a preloaded Jeffcott rotor. Chaos, Solitons and Fractals 15, 407–416 (2003)
32. Karpenko, E.V., Wiercigroch, M., Cartmell, M.P.: Regular and chaotic dynamics of a discontinuously nonlinear rotor system. Chaos, Solitons and Fractals 13, 1231–1242 (2002)
33. Karpenko, E., Wiercigroch, M., Pavlovskaia, E.E., Cartmell, M.P.: Piecewise approximate solutions for a Jeffcott rotor with a snubber ring. International Journal of Mechanical Sciences 44, 475–488 (2002)

34. Karpenko, E.V., Wiercigroch, M., Pavlovskaia, E.E., Neilson, R.D.: Experimental verification of Jeffcott rotor model with preloaded snubber ring. Journal of Sound and Vibration 298, 907–917 (2006)
35. Krivtsov, A.M., Wiercigroch, M.: Dry friction model of percussive drilling. Meccanica 34, 425–435 (1999)
36. Krivtsov, A.M., Wiercigroch, M.: Penetration rate prediction for percussive drilling via dry friction model. Chaos, Solitons and Fractals 11, 2479–2485 (2000)
37. Kunze, M.: Non-Smooth Dynamical Systems. Springer, New York (2000)
38. Litak, G., Friswell, M.I.: Dynamics of a gear system with faults in meshing stiffness. Nonlinear Dynamics 41, 415–421 (2005)
39. Lok, H.P., Neilson, R.D., Rodger, A.A.: Computer-based model of vibro-impact driving. In: Proceedings of ASME DETC: Symposium on Nonlinear Dynamics in Engineering Systems, Las Vegas (1999)
40. Muszynska, A., Goldman, P.: Chaotic responses of unbalanced rotor/bearing/stator systems with looseness or rubs. Chaos, Solitons and Fractals 5(9), 1683–1704 (1995)
41. Natsiavas, S.: Periodic response and stability of oscillators with symmetric trilinear restoring force. Journal of Sound and Vibration 134(2), 313–331 (1989)
42. Pavlovskaia, E., Wiercigroch, M.: Periodic solutions finder for vibro-impact oscillator with a drift. Journal of Sound and Vibration 267, 893–911 (2003)
43. Pavlovskaia, E., Wiercigroch, M.: Analytical drift reconstruction for impact oscillator with drift. Chaos, Solitons and Fractals 19(1), 151–161 (2004)
44. Pavlovskaia, E.E., Wiercigroch, M.: Low dimensional maps for piecewise smooth oscillators. Journal of Sound and Vibration 305(4-5), 750–771 (2007)
45. Pavlovskaia, E., Karpenko, E.V., Wiercigroch, M.: Nonlinear dynamic interactions of a Jeffcott rotor with a preloaded snubber ring. Journal of Sound and Vibration 276, 361–379 (2004)
46. Pavlovskaia, E., Wiercigroch, M., Grebogi, C.: Modeling of an impact system with a drift. Physical Review E 64, 56224 (2001)
47. Pavlovskaia, E., Wiercigroch, M., Grebogi, C.: Two dimensional map for impact oscillator with drift. Physical Review E 70, 36201 (2004)
48. Pavlovskaia, E.E., Wiercigroch, M., Woo, K.-C., Rodger, A.A.: Modelling of ground moling dynamics by an impact oscillator with a frictional slider. Meccanica 38, 85–97 (2003)
49. Peterka, F., Vacik, J.: Transition to chaotic motion in mechanical systems with impacts. Journal of Sound and Vibration 154(1), 95–115 (1992)
50. Rodger, A.A., Littlejohn, G.S.: A study of vibratory driving in granular soils. Geotechnique 30, 269–293 (1980)
51. Shaw, S.W., Holmes, P.J.: A periodically forced piecewise linear oscillator. Journal of Sound and Vibration 90(1), 129–155 (1983)
52. Shen, M.-H.H., Chu, Y.C.: Vibrations of beams with a fatigue crack. Computers & Structures 45, 79–93 (1992)
53. Sin, V.M.T., Wiercigroch, M.: A symmetrically piecewise linear oscillator: design and measurement. Proceeding of the Insitute of Mechanical Engineers Part C 213, 241–249 (1999)
54. Spektor, M.: Principles of Soil Tool Interaction. Journal of Terramechanics 18, 51–65 (1981)
55. Wiercigroch, M.: Comments on the study of a harmonically excited linear oscillator with a Coulomb damper. Journal of Sound and Vibration 167, 560–563 (1993)
56. Wiercigroch, M.: Dynamics of discrete mechanical system with discontinuities, p. 127. Silesian Universtity Press, Gliwice (in Polish)

57. Wiercigroch, M.: Chaotic vibrations of a simple model of the machine tool-cutting process system. Journal of Vibration and Acoustics Trans. ASME 119(3), 468–475 (1997)
58. Wiercigroch, M.: Modelling of dynamical systems with motion dependent discontinuities. Chaos, Solitons and Fractals 11(15), 2429–2442 (2000)
59. Wiercigroch, M.: Applied nonlinear dynamics of non-smooth mechanical systems. Journal of the Brazilian Society of Mechanical Sciences and Engineering XXVIII (4), 519–526 (2006)
60. Wiercigroch, M., de Kraker, B. (eds.): Applied nonlinear dynamics and chaos of mechanical systems with discontinuities. Nonlinear Science Series A. World Scientific, Singapore (2000)
61. Wiercigroch, M., Pavlovskaia, E.E.: Nonlinear dynamics of vibro-impact systems: theory and experiments. In: Glasgow, Cartmell, M. (eds.) Proceedings of the 5th International Conference on Modern Practice in Stress and Vibration Analysis, September 9-11, pp. 513–520 (2003)
62. Wiercigroch, M., Sin, V.M.T.: Experimental study of base excited symmetrically piecewise linear oscillator. Journal of Applied Mechanics, Trans. ASME 65, 657–663 (1998)
63. Wiercigroch, M., Sin, W.T.V., Li, K.: Measurement of chaotic vibration in symmetrically piecewise linear oscillator. Chaos, Solitons and Fractals 9(1-2), 209–220 (1998)
64. Wiesenfeld, K., Tufillaro, N.B.: Suppression of period doubling in the dynamics of a bouncing ball. Physica D 26, 321–335 (1987)
65. Yorke, J.A., Nusse, H.E.: Dynamics. Springer, New York (1998)
66. Zastrau, B.: Vibration of cracked structures. Archive of Mechanics 37, 736–743 (1985)